Eur. Phys. J. A (2014) **50**: 128
DOI 10.1140/epja/i2014-14128-4

THE EUROPEAN PHYSICAL JOURNAL A

Review

The Radioactive Ion Beams in Brazil (RIBRAS) facility

Description, program, main results, future plans

A. Lépine-Szily[a], R. Lichtenthäler, and V. Guimarães

Instituto de Física da Universidade de São Paulo, Caixa Postal 66318, 05314-0970, São Paulo, SP, Brazil

Received: 17 April 2014 / Revised: 2 July 2014
Published online: 21 August 2014 – © Società Italiana di Fisica / Springer-Verlag 2014
Communicated by N. Alamanos

Abstract. RIBRAS (Radioactive Ion Beams in Brazil) is a facility installed at the Institute of Physics of the University of São Paulo (IFUSP), Brazil. The RIBRAS system consists of two superconducting solenoids and uses the "in-flight method" to produce radioactive ion beams using the primary beam provided by the 8UD Pelletron Tandem of IFUSP. The ion beams produced so far by RIBRAS are ^{6}He, ^{8}Li, ^{7}Be, ^{10}Be, ^{8}B, ^{12}B with intensities that can vary from 10^4 to 10^6 pps. Initially the experimental program covered the study of elastic and inelastic scattering with the objective to study the interaction potential and the reaction mechanisms between weakly bound (RIB) and halo (^{6}He and ^{8}B) projectiles on light, medium and heavy mass targets. With highly purified beams, the study of resonant elastic scattering and resonant transfer reactions, using inverse kinematics and thick targets, has also been included in our experimental program. Also, transfer reactions of astrophysical interest and fusion reactions induced by halo nuclei are part of the near-future research program. Our recent results on elastic scattering, alpha-particle production and total reaction cross sections, as well as the resonant elastic and transfer reactions, are presented. Our plans for the near future are related to the installation of a new beam line and a cave for gamma-ray detection. We intend to place in operation a large area neutron detector available in our laboratory. The long-range plans could be the move of the RIBRAS system to the more energetic beam line of the LINAC post-accelerator (10 MeV/nucleon primary beams) still in construction in our laboratory.

1 Introduction

The atomic nucleus is a quantum many-body system governed by the strong interaction. One of the main goals of nuclear physics is the establishment of a complete and predictive theory of complex nuclei. An essential part of this study is about the understanding of the collective and single particle aspects and their correlations, to allow a unique microscopic description of all aspects. This quest has led to the development of radioactive beams since they permit an expansion from the one-dimensional image, where only the nuclear mass is varied, to a two-dimensional one, where the proton number Z as well as the neutron number A-Z can vary over a wide range. The atomic nucleus has proved to be a useful laboratory for tests of many kinds of new phenomena: for instance, very neutron-rich nuclei allow the study of unusual properties of weakly bound quantum systems, such as the nuclear halo [1, 2]. Nuclei far from the stability line also present changes in the shell structure, with new magic numbers [3, 4].

Great progress in our understanding of nuclear structure is due to experiments performed in many laboratories using radioactive ion beams (RIB). Before the use of RIB, knowledge of nuclear structure and reactions was based on experiments using systems of stable or very long-lived nuclei. However, more than 90% of all nuclei, most of them still unknown, are located between the stability line and the drip lines, where many new phenomena can take place.

Radioactive ion beams can be produced by several reaction mechanisms, such as in-flight fragmentation of the projectile, spallation or target fragmentation followed by the isotope separation online (ISOL) method, transfer reactions, fusion, or even fission [5]. The first two processes occur at intermediate and high incident energies and are used at many large laboratories around the world. They have the advantages of high intensity, can produce light and heavy radioactive beams, and the possibility to move further away from the stability valley. The use of transfer reactions to produce RIB is possible at much lower energies and, in this way, small laboratories with quite low-energy accelerators, are also making important contributions in this field. Their main advantage is that they produce low-energy RIB. At energies near the Coulomb barrier or above, valuable information on the structure of exotic nuclei and on the dynamics of the nuclear reactions between them can be obtained. Important issues, such as fusion below the Coulomb barrier, and the role

[a] e-mail: alinka@if.usp.br

of the neutron halo with respect to fusion, can be studied only with low-energy beams. Many experiments were performed with light exotic nuclei presenting halo, such as ^{6}He, ^{8}He, ^{11}Li, or ^{11}Be among others [6]. On the other hand, recent experiments with radioactive ion beams have been very successful in nuclear astrophysics investigations, where many stellar scenarios involve short-lived nuclei [7].

In the late nineties, our laboratory decided to extend the capabilities of the Pelletron Tandem - 8UD, installed at the Institute of Physics of the University of São Paulo (IFUSP), by producing secondary beams of radioactive nuclei. The 8UD Tandem is the only particle accelerator in Brazil contributing significantly to the development of fundamental research in nuclear physics. The Radioactive Ion Beams in Brazil (RIBRAS) system is the first to produce secondary beams of unstable nuclei in the Southern Hemisphere and it is the only one in Latin America. In operation since 2004, it has been working continuously since then.

Until recently almost all experiments performed at RIBRAS were on elastic scattering. Elastic scattering angular distributions were measured for the available radioactive beams (^{6}He, ^{8}Li, ^{7,10}Be and ^{8}B) on light, medium mass and heavy targets at various energies, near and above the Coulomb barrier. These measurements are important since they allow the determination of the optical potentials between the radioactive projectiles and the targets. These can be quite different from those of stable systems due to the halo structure or the low binding energy of the radioactive nuclei. The elastic scattering also gives information on the total reaction cross section and on the size of the nuclei involved. The coupling of the elastic scattering to other important channels, as breakup or transfer, can also be investigated through the elastic scattering experiments. In the case of radioactive projectiles, these effects are strongly enhanced and their study as a function of the target mass or the incident energy was achieved by our measurements. This review intends to give a description of the experimental device, of the scientific results achieved, and of future plans.

2 Description of the Radioactive Ion Beams in Brazil (RIBRAS) facility and ancillary equipments

The Radioactive Ion Beams in Brazil (RIBRAS) [8] is a system based on superconducting solenoids to produce secondary beams of unstable nuclei. It is installed in the Open Laboratory of Nuclear Physics (LAFN) at the Physics Institute of the University of São Paulo (IFUSP) in São Paulo, Brazil. The choice for a solenoid based system was based on the successful example of the TWINSOL facility [9] installed at the University of Notre Dame, USA. However, due to the future perspective of a LINAC post-accelerator installation in our laboratory, which would produce primary beams with $E \leq 10\,\mathrm{MeV/nucleon}$, the solenoids were designed to take into account the higher-energy beams to be delivered.

To produce the secondary radioactive beams, the RIBRAS system uses the "in-flight method", where the radioactive beams are produced on-line by a nuclear reaction (one or two-nucleon transfer reactions), triggered by a stable primary beam on a stable target. The continuous stable beams are accelerated by the long standing 8UD Pelletron Tandem accelerator of the LAFN [10]. The term 8UD refers to eight electrostatic accelerating units arranged in tandem configuration on both sides of the high voltage terminal which can reach 8 MV. Beams of protons, deuterons, Li, Be, B, C, O, F, Si isotopes and heavier ions up to Cu, with typical intensities around μAe, can be delivered. The maximum energies are between 2–5 MeV/nucleon. The superconducting LINAC in installation will raise the energy of the stable beams to 10 MeV/nucleon. Also, pulsed beams of Li, Be, B, C, O isotopes, and heavier beams will be available with the completion of the LINAC post-accelerator.

2.1 Description of the solenoids and production targets

The RIBRAS system consists of two large air-core (30 cm clear warm bore), superconducting solenoids with 6.5 T maximum central field (5 Tm axial field integral). The system has three chambers, one before the first solenoid (small ISO chamber) that will be called chamber-1. A central scattering chamber (25 cm diameter ISO chamber) located between the two solenoids will be called chamber-2. Recently a new, large (70 cm diameter) scattering chamber was installed after the second solenoid, that will be named chamber-3. See fig. 1 for a schematic view of the system. The superconducting solenoids were manufactured by Cryomagnetics Inc. (USA). The magnet coils are immersed in a liquid-helium (LHe) dewar which contains a maximum of 250 l of LHe, with a boil-off rate of 2–3 liters/day. The LHe vessel is surrounded by a liquid-nitrogen vessel of 130 l and vacuum shields to minimize the LHe consumption. This vessel configuration, associated with the option of the persistent mode, allows an economical operation of the solenoids. The helium gas evaporating from the dewars is recovered, compressed into cylinders, and liquified at IFUSP. Also, the solenoids have no external iron yoke, so there is a weak external magnetic field. The two superconducting solenoids act as thick lenses to collect, select, and focus the secondary beam. With the large bore of the solenoids, it is possible to reach a large angular acceptance, $2^\circ \leq \theta \leq 15^\circ$, *i.e.*, about 30 msr in solid angle, in comparison with about 5 msr which can be obtained from a dipole based system.

The production system (primary target) consists of a gas cell, mounted in chamber-1, before the first solenoid. The primary target can be a gas or a solid target, such as a ^{9}Be foil, which is mounted as the gas cell window. The ^{9}Be foil is commercial, with a nominal thickness of 12 μm. Before using it, we usually measure its thickness by the energy loss of the α-particles emitted by a ^{241}Am source. In the case of using a solid foil target, the gas inside the cell would have the purpose of cooling the foil heated by the primary beam. In other situations, the gas inside the

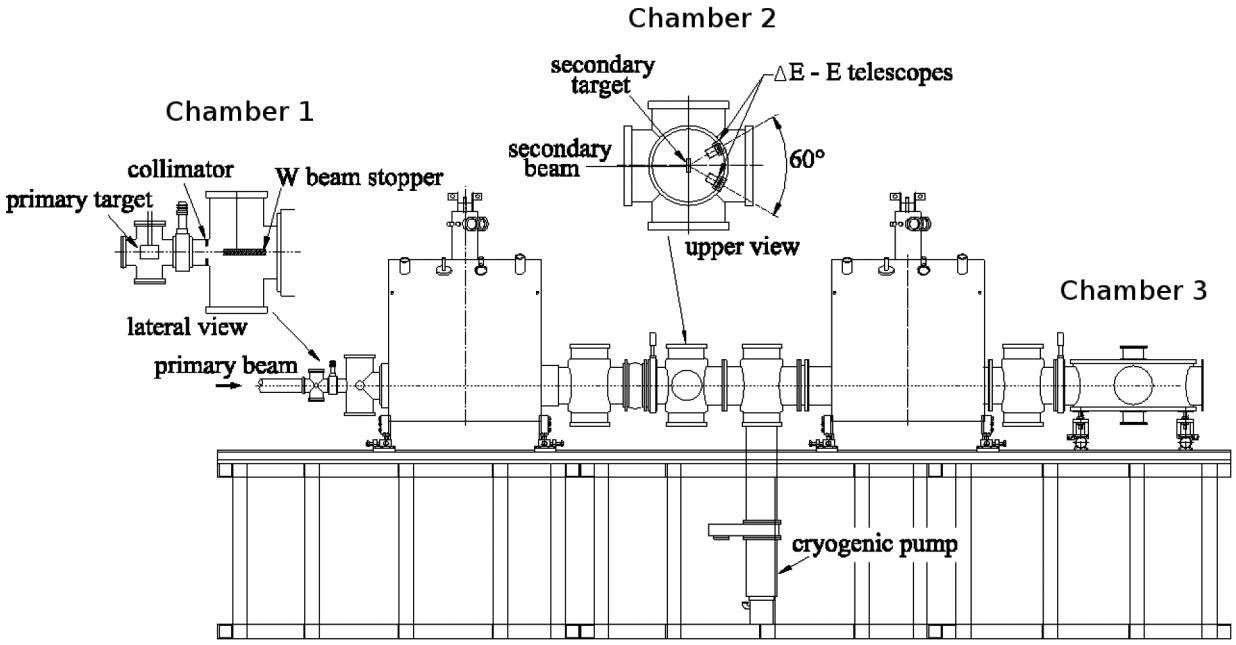

Fig. 1. The experimental set-up of RIBRAS: the stable beam comes from the left, the production target, located in chamber-1 is followed by the W beam stopper and the first solenoid, which is followed by the central scattering chamber-2, with the secondary target and detectors installed in it, followed by the second solenoid and the large scattering chamber-3. Taken from ref. [11].

cell can be used as the production target and, in this case, the entrance and exit windows can be just thin vacuum-tight metal foils. Tens of centimeters downstream, in the beam line after the gas cell, there is a tungsten rod with electron suppression and with a cylindrical hole (geometrical suppression) to stop and collect the primary beam particles (Faraday cup). The Faraday cup not only stops the primary beam but also the secondary beams in the angular range between zero and 2°. A current integrator connected to the Faraday cup measures the total incident charge during a run.

The first solenoid makes an in-flight selection by the magnetic rigidity of the reaction products emerging from the primary target in the forward angle region. As the first magnet focuses all ions with the same magnetic rigidity, *i.e.*, the same ME/Q^2 ratio, where M, E and Q stand for mass, energy, and charge state of the ion, the beam of interest can be accompanied by many contaminant beams of the same magnetic rigidity, but with different charges, masses and energies. A collimator at the entrance of the first solenoid limits the maximum angular acceptance to 6°, so, in this set-up, the angular divergence of the secondary beams entering the first solenoid is 4°, between 2° and 6°. The angular divergence of the secondary beam in chamber-2 is 3.2°, between 1.3° and 4.5°.

2.2 Production of radioactive ion beams

The production of radioactive ion beams (RIB) depends on the combination of the nuclear reaction, which produces the radioactive nucleus of interest, and of the system used to select and focus the secondary beam. At low energies ($E \leq 10\,\mathrm{MeV/nucleon}$), selective reactions have to be chosen, such as few nucleon transfer reactions, fusion or breakup reactions, preferably with a forward-peaked cross section. To transfer as much as possible of the projectile energy to the secondary beam, it is useful to use reactions in inverse kinematics (heavy beam on a light target). Also, the primary beam has to be intense ($\geq 0.5\,\mu$A) and the production target must be robust enough to withstand it.

For primary stable beams at energies such as those delivered by our Pelletron accelerator, transfer reactions are the best options to produce radioactive nuclear beams. Cross sections for one- or two-nucleon transfer reactions are on the order of 10-20 mb. Also, transfer reactions with large forward-peaked cross sections in the angular range of 2° to 6°, which is the angular acceptance of RIBRAS, are required to obtain useful secondary beam intensities. Usually, many different species are produced with similar intensities in the production target and the beam of interest has to be selected and focused by an electromagnetic selector device, a solenoid in our case. If the production reaction occurs in inverse kinematics with a heavier primary beam hitting a light production target, the kinematic focusing is better.

The main advantages of this system is that it can be used to produce very short-lived species. Depending on the reaction and element produced, the secondary beam can have a quite favorable intensity. The energy control for the primary beam of the Pelletron tandem allows for very low energy of the secondary beam, which is an advantage for reactions of astrophysical interest. The disadvantages are the secondary beam quality and purity, which

Table 1. Secondary beams produced at the RIBRAS facility and the nuclear reactions used for their production. The intensities, purities, energy resolution (FWHM) and energies obtained for the beams at the chamber-2 are also shown. The intensities are reported in pps per 1 μA of primary beam.

Secondary beam	Production reaction	Q-value (MeV)	Intensity (pps)	Energy resolution FWHM (keV)/Energy	Purity %
^{6}He	^{9}Be(^{7}Li, ^{6}He)^{10}B	−3.390	10^5–10^6	1000/22 MeV	16
^{7}Be	^{3}He(^{6}Li, ^{7}Be)d	+0.112	10^4–10^5	800/18.8 MeV	2
^{7}Be	^{7}Li(^{6}Li, ^{7}Be)^{6}He	−4.369	10^4–10^5	1000/22 MeV	2
^{8}Li	^{9}Be(^{7}Li, ^{8}Li)^{8}Be	+0.367	10^5–10^6	500/25.8 MeV	44
^{8}B	^{3}He(^{6}Li, ^{8}B)n	−1.975	10^4	1000/15.6 MeV	4.4
^{10}Be	^{9}Be(^{11}B, ^{10}Be)^{10}B	−4.642	10^5	800/23.2 MeV	3
^{12}B	^{9}Be(^{11}B, ^{12}B)^{8}Be	+1.705	10^5	800/25.0 MeV	

are not excellent, and the limitation to radioactive species not very far from the stability valley. As examples, the one-nucleon transfer reactions used for the solenoid based system are ^{9}Be(^{7}Li, ^{8}Li)^{8}Be and ^{9}Be(^{7}Li, ^{6}He)^{10}B, which produce reasonably intense beams of ^{8}Li (10^6 pps) and ^{6}He (10^5 pps) for 1 μA of primary beam. However, to produce the radioactive proton-rich ^{8}B beam, it is necessary to use a two-proton transfer reaction, such as ^{3}He(^{6}Li, ^{8}B)n, where a ^{3}He gas cell is required and a lower intensity is obtained, 10^4 pps (per 1 μA of the ^{6}Li primary beam).

2.3 Secondary beams already produced (intensities, production reactions, production rates)

The secondary radioactive ion beams already produced with the RIBRAS system are presented in table 1, together with the nuclear reaction used for their production. As mentioned above, the solenoid makes a magnetic rigidity selection and nuclei with the same $B\rho$ are transmitted and focused together with the beam of interest. Some examples of these contaminant beams are presented in figs. 2, 3 and 4. These two-dimensional $E-\Delta E$ identification spectra were measured in chamber-2 with a $\Delta E-E$ Si telescope with the beams hitting a heavy (usually gold) secondary target.

Figures 2, 3, and 4 clearly show that the main contaminant beams, measured in chamber-2, are the degraded primary beam in a lower charge state and ^{4}He, as well as light particles, such as protons, deuterons, and tritons. The fully stripped primary beam ^{7}Li^{3+} has a smaller magnetic rigidity than the fully stripped ^{6}He^{2+} or ^{8}Li^{3+} secondary beams and consequently, its focal point is located before the secondary beams of interest. Thus, it can be stopped in a blocker located at its crossover point, before the secondary target and is not observed in our spectra. However, the degraded primary beam in the 2^+ charge state has a continuous energy distribution and can be focused with the beam of interest at any $B\rho$-value. The same argument applies for the ^{4}He contaminant beam. The ^{9}Be target can break into two ^{4}He+n and these α-particles have a continuous energy distribution, observable at any magnetic rigidity. Light particles such as protons, deuterons and tritons, degraded after the production tar-

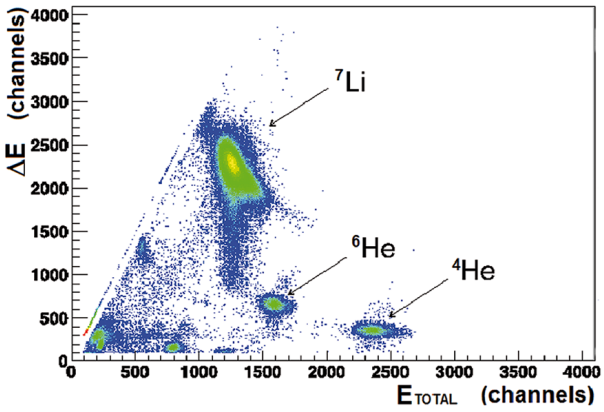

Fig. 2. Two-dimensional $E-\Delta E$ identification spectrum obtained using a $E-\Delta E$ Si telescope in chamber-2, with the ^{6}He secondary beam focused on a gold target. The production reaction was ^{9}Be(^{7}Li, ^{6}He)^{10}B and the energy of the ^{6}He beam was 16.2 MeV. The contaminant beams are ^{7}Li^{2+}, ^{4}He, protons and deuterons. The relative intensity of the beam of interest, ^{6}He, was 16%. Taken from ref. [12].

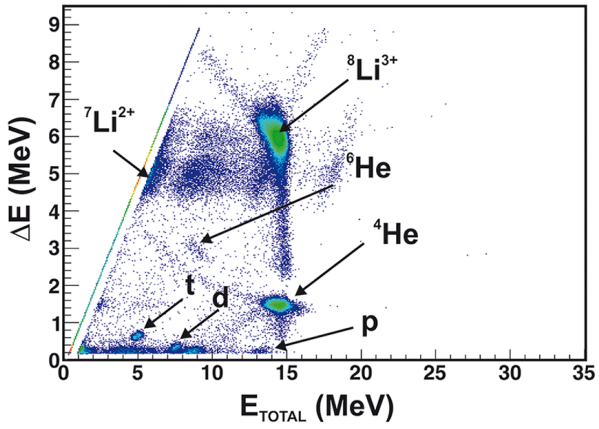

Fig. 3. Two-dimensional $E-\Delta E$ identification spectrum obtained using a $E-\Delta E$ Si telescope in the chamber-2, with the ^{8}Li secondary beam focused on a gold target. The production reaction was ^{9}Be(^{7}Li, ^{8}Li)^{8}Be and the energy of the ^{8}Li beam was 19.0 MeV. The contaminant beams are ^{7}Li^{2+} (38%), ^{4}He (16%), protons, deuterons, tritons and ^{6}He, any of them less than 1%. The relative intensity of the beam of interest, ^{8}Li, was about 44%. Taken from ref. [13].

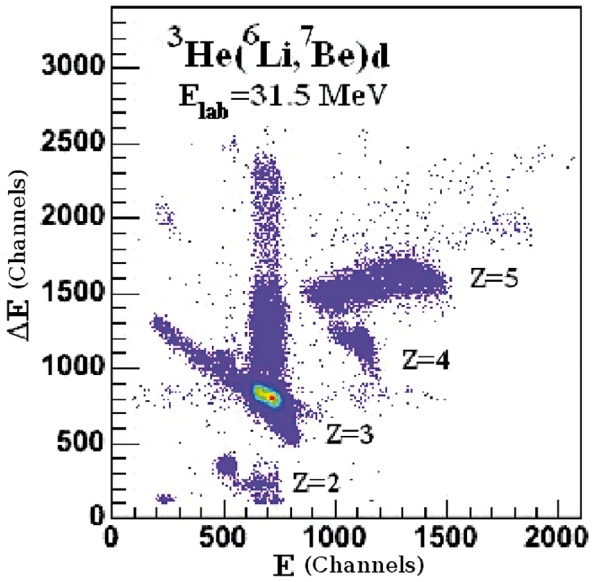

Fig. 4. Two-dimensional $E - \Delta E$ identification spectrum obtained using an $E - \Delta E$ Si telescope in chamber-2, with the ^{7}Be and ^{8}B secondary beams focused on a gold target. The contaminant beams are $^6Li^{2+}$ and ^{4}He.

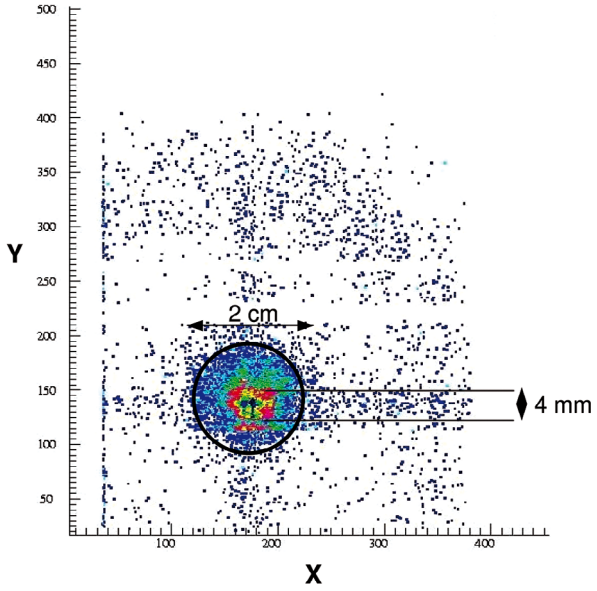

Fig. 5. The beam profile in the center of chamber-2 was measured using an x-y position-sensitive parallel plate avalanche counter (PPAC) in coincidence with a Si detector located behind the PPAC. We obtained a well-centered circular spot of about 4 mm of diameter indicated in this figure.

get, are also focused at any selected magnetic rigidity and are present in our spectra. In the case of focusing the ^{8}Li secondary beam, it is about 44% of the total beam intensity in chamber-2. In the case of the ^{6}He secondary beam, it is only about 16% of the total secondary beam intensity. The elastic cross sections of the beam of interest and the different contaminants, scattered on the Au target, were taken into account to calculate the relative purities in the cases we used the scattered beam. In some cases, we performed measurements of the secondary beam and contaminant intensities by placing a detector at zero degrees, directly on the secondary beam, and reducing the beam to intensities below 1 nAe. In case of the ^{7}Be and ^{8}B secondary beams, the primary beam is $^6Li^{3+}$ which has a magnetic rigidity higher than the secondary beams of interest, which are proton rich and have low magnetic rigidity due to their high charge state. As a consequence, particles of $^6Li^{3+}$, and others with degraded energy, can fall into the band pass of the solenoid, producing more contaminated spectra in chamber-2 (see fig. 4), than in the case of neutron-rich beams, such as, ^{6}He and ^{8}Li. In the next subsection, the purification of secondary beams is discussed.

The energy resolution of the different secondary beams in chamber-2 is quoted in table 1 and it is the full width at half maximum (FWHM) of the elastic peaks on a gold target, measured at forward angles. It varies between 500 and 1000 keV of FWHM at incident energies of about 20–25 MeV. The corresponding standard deviation σ is this value divided by 2.35, and thus, smaller. It depends on many factors, such as the kinematics of the production reaction and the kinematic broadening due to the angular divergence, as well as the thickness of the production target and the energy straggling inside it.

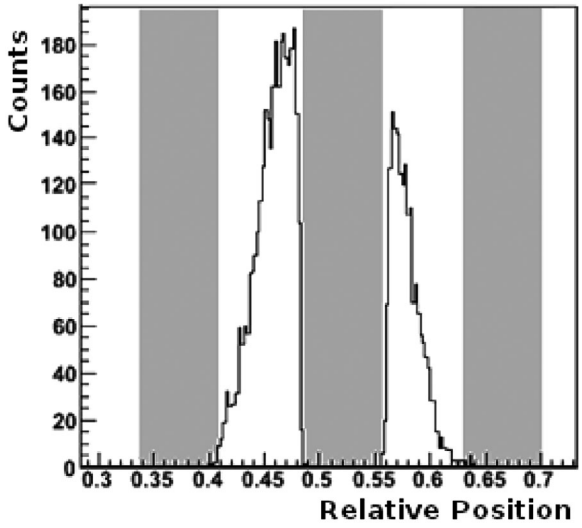

Fig. 6. The beam profile on the horizontal-axis at the center of chamber-2 was measured using a position sensitive (PSD) silicon detector. We obtained a perfectly centered spot of 3.5–4 mm indicated in this figure.

The beam profile at the center of chamber-2 was checked by different methods: i) measuring with an x-y position-sensitive parallel plate avalanche counter (PPAC), we obtained a well-centered circular spot of about 4 mm in diameter, shown in fig. 5; ii) using a TIMEPIX detector [14], we obtained a similar result; however, the TIMEPIX detector was not mounted exactly at the center of chamber-2 in the case of the measurement; iii) more recently, by using a position-sensitive (PSD) silicon detector on the horizontal axis, a perfectly centered spot of 3.5–4 mm was observed, shown in fig. 6.

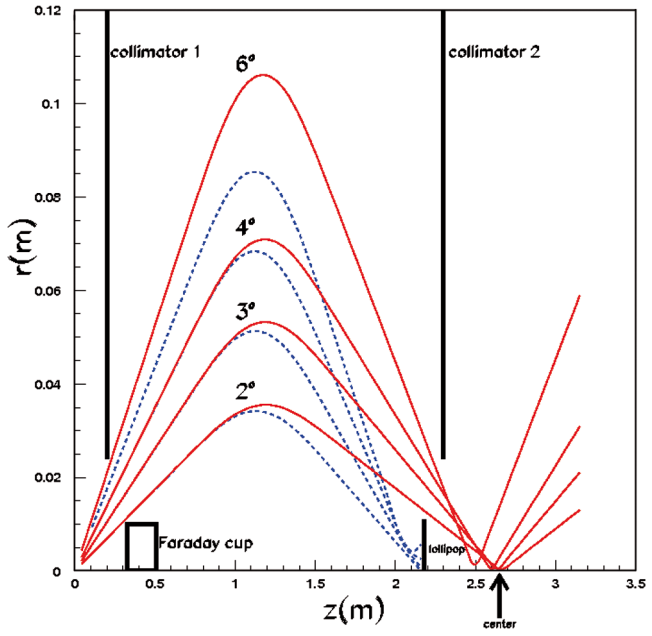

Fig. 7. The trajectories calculated by the code TwinSol, for ^{8}Li beam (red solid line) and the primary beam ^{7}Li (blue dotted line), which is stopped by a blocker positioned at its focal point.

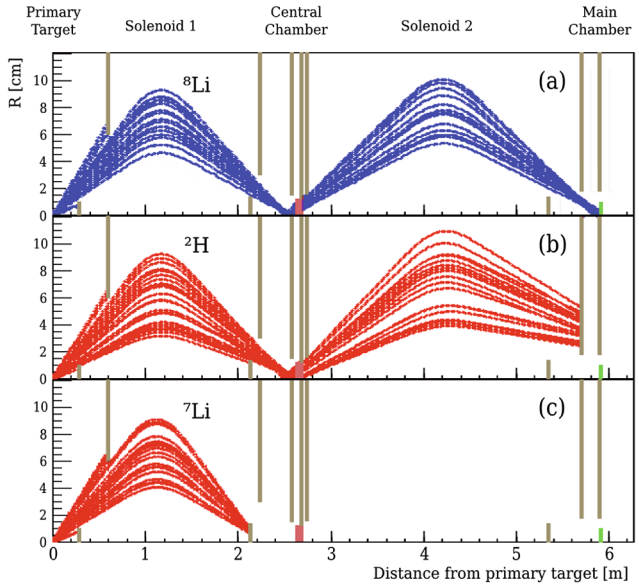

Fig. 8. The trajectories calculated by the code SolFocus for the two solenoids, with a degrader in chamber-2, for ^{8}Li beam (blue solid line in (a)), for the contaminant beam ^{2}H (red solid line in (b) and the primary beam ^{7}Li (red solid line in (c)), which is stopped by a blocker positioned at its focal point.

2.4 Purification of the secondary beams (collimators, blockers, degrader systems, timing measurements)

The purity of the secondary radioactive beam is attained by a system of blockers and collimators strategically positioned along the RIBRAS beam line. The blockers are circular obstacles (*lollipop*) and can be conveniently positioned at any point along the beam axis. The blockers should be placed at the focus of the main contaminant beams. The collimators limit the angular range and cut contaminants that have angular ranges larger than the beam of interest.

We have the option of two codes to calculate the trajectory of the particles through the solenoids. The first one, which only calculates trajectories, is a `fortran-90` computer code, first developed for the TwinSol system of the University of Notre Dame, USA [15], and then adapted for the RIBRAS magnets [16]. This program integrates numerically the equation of movement of a particle, given its mass, charge state, velocity and the magnetic field at each point of the trajectory, from the primary target up to the focusing position. An example of the trajectories calculated for $^{8}Li^{3+}$ and the contaminant $^{7}Li^{3+}$ for the first solenoid is shown in fig. 7.

The second code is SIM-RIBRAS [17], a ROOT-based [18] set of Monte Carlo routines specially designed to provide support for experiment planning and experimental setup enhancing, which gives a complete simulation of the experiment. It has two main programs: CineRIBRAS, which performs beam kinematics simulations, with energy absorbers, and SolFocus, which calculates the beam selection and focusing in RIBRAS. With a full description of RIBRAS's geometry, magnetic field and secondary beam selection, it searches for the optimal electric current in the solenoids, providing beam tracks and beam spots at the focal planes. It also calculates the possible contaminant beams and allows the inclusion of collimators, blockers and degraders. An example of trajectories calculated by SolFocus is presented in fig. 8.

The use of two magnets in RIBRAS is important to purify the secondary beams. With two solenoids, it is possible to use the differential energy loss in an energy degrader foil, located at the crossover point between the magnets, to select the ion of interest and move the contaminant ions out of the band pass of the second solenoid. Choosing the magnetic field in the second solenoid to focus the secondary beam of interest, the contaminant beams, which have different magnetic rigidity after the degrader, are no longer focused. Some collimators are mounted along the beam line, allowing only the beam particles which hit the degrader at the cross over point to traverse the second solenoid. This method, however, does not provide good separation of the isotopes.

In order to obtain the best beam purification, degraders of different materials, such as Al, Au, kapton and $[CH_2]_n$ polyethylene foils, were tested. Two-dimensional spectra of a Si detector telescope, presented in fig. 9, show that the purity of the ^{8}Li beams in chamber-3 is about 99% when using a degrader in chamber-2. It should be compared with a purity of 65%, obtained without the use of a degrader. This result was obtained using a $[CH_2]_n$ polyethylene foil of convenient thickness as degrader and the secondary beam was scattered on a gold target at the center of chamber-3 and detected at $\theta_{lab} = 10^{\circ}$ using a $E - \Delta E$ Si detector telescope. If we compare fig. 3, measured in chamber-2, and fig. 9(a), measured in chamber-3,

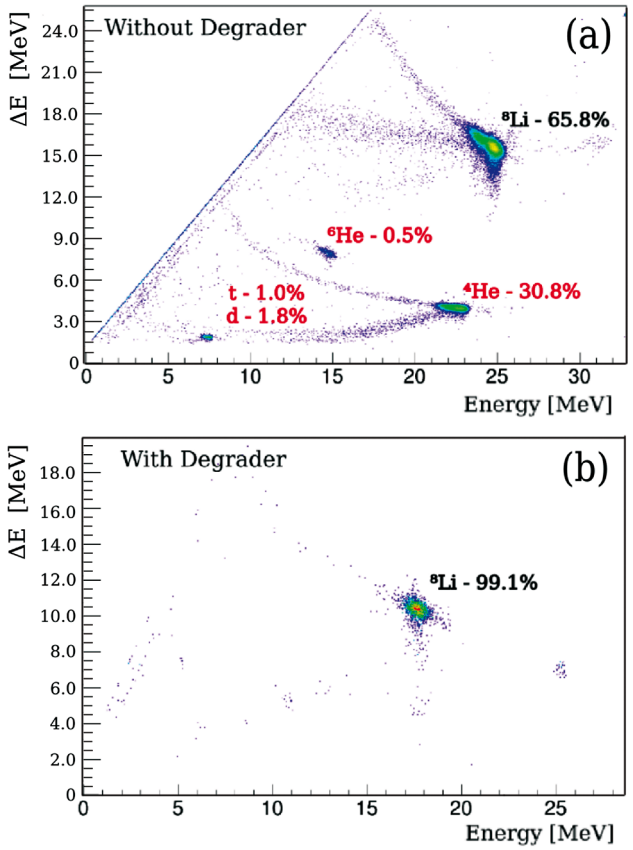

Fig. 9. Two-dimensional $E - \Delta E$ identification spectra obtained using a Si telescope at $\Theta_{\rm lab} = 10^{\circ}$, in chamber-3, with the ^{8}Li secondary beam focused on a gold target. Spectrum (a) was obtained without a degrader and spectrum (b) with a degrader in chamber-2.

both without degrader, we see that in chamber-3 the $^{7}Li^{2+}$ has been practically removed by collimators and blockers placed between the two chambers and the purity of ^{8}Li, which was 44% in chamber-2, has increased to 65% in chamber-3. The transmission from chamber-2 to chamber-3, for the ^{8}Li beam, using degrader, was about 50%.

For the ^{6}He secondary beam, a purification from 16% in chamber-2 to 92% in chamber-3 was obtained by using a $[CH_2]_n$ foil of 12 μm as a degrader placed in chamber-2 [19].

In the following sect. 4, it will be shown that even with a cocktail of secondary beams (beam of interest plus many contaminant beams), the elastic scattering measurements in direct kinematics (target heavier than beam) can be performed, since the elastic scattering peaks are well separated and easily identified. This is the main reason why we performed only elastic scattering angular distribution measurement during the period when chamber-3 was not operational. For these measurements, the purification, which reduces the beam intensity, is unnecessary. However, for reactions, such as transfer, fusion, and even for inverse kinematic elastic scattering (see sect. 6), where, in the identification spectrum, the reaction products of interest can be superimposed on contaminants, the purification is essential.

An additional cleaning of the secondary beam, especially useful to separate isotopes, can be obtained by using a time-of-flight (TOF) technique, for which a pulsed primary beam would be very useful. The TOF can also be determined using two timing detectors some meters apart. Recently, a timing detector, based on a microchannel plate detector (MCP) was developed and installed in chamber-2. The other timing signal should be given by the fast signal of the surface barrier Si E detector of the telescope in chamber-3. This system was recently tested; the efficiency of the time detector for the 5.486 MeV α-particles of a ^{241}Am source was 85%. However, when using a ^{8}Li beam and degrader, the efficiency was lower, due to the residual magnetic fields of the magnets. Due to the use of a degrader, the magnetic fields in the two solenoids were different and did not cancel out at the location of the MCP detector. In the future, magnetic shielding will be placed around the MCP detector to improve its efficiency. The beam profile was measured with a PSD detector mounted at the center of chamber-3 on the horizontal direction; the diameter of the beam spot was 6.5–7 mm.

The installation of a pulsed primary beam in our Pelletron accelerator would greatly improve the beam purity and selection of the secondary particles produced by RIBRAS. A pulsed primary beam would allow the measurement of the time of flight (TOF) between the primary beam and the detectors after the secondary target and would provide means to select different secondary particles by their different TOF. The installation of a beam buncher with a frequency compatible with the LINAC post-accelerator under construction is underway in our Pelletron accelerator.

3 Elastic scattering measurements

3.1 Introduction

With this equipment in operation since 2004, we have performed systematic studies of elastic scattering and reactions of exotic nuclei on targets of various masses [12, 13, 20–28]. Below, we discuss some aspects of this research based on experimental data obtained at RIBRAS. Elastic scattering is the simplest process that can occur in the collision of two nuclei. The kinetic energy and angular momentum are conserved, as well as the identity of the colliding nuclei. At low energies, it is the most important process in terms of cross section and provides information on the nuclear potential, as well as the total reaction cross section. In addition, angular distributions of elastic scattering may contain effects due to the coupling with other reaction channels, providing indirect information about these channels.

In the case of elastic scattering of stable projectiles, the angular distributions show a more or less typical pattern. At energies near the Coulomb barrier, the scattering is pure Rutherford in the forward angle region with $\sigma/\sigma_{\rm Ruth} \approx 1$. As the scattering angle is increased, the short-range nuclear force begins to act, and deviations

from the Rutherford cross section are observed [29]. These deviations basically consist of an oscillatory diffraction pattern, typical of a Fresnel diffraction, due to the interference between partial waves refracted, respectively, in the Coulomb and nuclear potentials, emerging at the same scattering angle. This kind of Coulomb rainbow is typical of heavy and intermediate mass systems at energies close to the Coulomb barrier. For larger angles, the absorptive component of the optical potential increases and the ratio of the elastic scattering to Rutherford cross section presents an exponential falloff. The angle at which the cross section falls to $\sigma/\sigma_{\rm Ruth} = 1/4$ is called $\theta_{1/4}$, and separates the illuminated and the shadow regions [30]. This angle is sometimes called the grazing scattering angle and can be related to the size of the system via the deflection function, which is known analytically for the case of pure Coulomb scattering. In a semi-classical view, the deflection function is a fundamental quantity, which relates the impact parameter, or the angular momentum of the incident particle, with the scattering angle. The grazing angular momentum is then related to the grazing scattering angle, or $\theta_{1/4}$ and, measurements of the differential scattering cross section, in a region around this angle, provide important information on the size of the system and the total reaction cross section.

As we go to lighter mass systems, the Coulomb barrier becomes lower and the diffraction pattern changes from the Fresnel to the Fraunhofer type with the appearance of oscillations in the angular distributions, whose periods are related to the grazing angular momentum of the collision.

In the case of exotic projectiles, some peculiarities have been observed. Due to the low binding energies of the projectiles compared to the stable isotopes, a strong coupling with states in the continuum, namely the breakup and neutron transfer, is expected. The low binding of the exotic projectiles makes them prone to breakup, even in the long-range Coulomb field of the target, which introduces a long-range component in the absorptive potential. In addition, some projectiles, such as ^{11}Li, ^{6}He, ^{11}Be, and others, present a neutron halo which enhances the probability of neutron transfer reactions, even at energies below the Coulomb barrier. Those processes are, in general, strongly coupled to the elastic scattering and introduce characteristic dynamic polarizations in the optical potential which are not present in the case of stable projectiles.

In the next subsections, we will present our experimental method and a theoretical description of the reaction models used in the analysis of our data. In sect. 4, we present the experimental data of the collision of exotic projectiles, such as ^{6}He, ^{8}Li, and ^{7,9,10}Be, on targets with different masses that illustrate these phenomena. ^{8}Li and ^{7}Be are radioactive and weakly bound nuclei; however, they do not present a halo structure. One of the main motivations to perform elastic scattering experiments with ^{8}Li and ^{7}Be beams was to observe any possible effect in the elastic data due to their different cluster configuration as compared to the configuration of ^{7}Li and ^{6}Li nuclei. The cluster structures and the binding energies (BE) of these four weakly bound nuclei are the following: $^{8}\mathrm{Li} \rightarrow {}^{7}\mathrm{Li} + \mathrm{n}$; BE = 2.033 MeV. $^{7}\mathrm{Li} \rightarrow {}^{4}\mathrm{He} + \mathrm{t}$; BE = 2.467 MeV. $^{6}\mathrm{Li} \rightarrow {}^{4}\mathrm{He} + \mathrm{d}$; BE = 1.474 MeV. $^{7}\mathrm{Be} \rightarrow {}^{4}\mathrm{He} + {}^{3}\mathrm{He}$; BE = 1.586 MeV. As the cluster structures are quite different, going from a valence neutron + ^{7}Li core to two He isotopes, it would be interesting to see how the different mechanism (transfer and breakup) would compete with the elastic scattering on the same target due to different configurations of the projectiles. For instance, for nuclei with a valence neutron, such as ^{8}Li, only the core would be affected by the Coulomb field of the target, while for nuclei, such as ^{7}Be, ^{7}Li, and ^{6}Li, both cluster particles would be affected by the Coulomb field. In this case, what would be more important for the breakup; the low binding energy or the possibility to produce dipole polarization? Of course, the point here is whether one could observe these effects or not in the elastic scattering or in some other specific reaction mechanism and, that is why these experiments were conducted with the RIBRAS system. Moreover, this kind of experiment, induced by only modestly exotic beams, could be very suitable for small laboratories as the one in São Paulo, where there is a tradition of making available longer beam times for lower count rates.

3.2 Experimental methods

Most of the elastic scattering experiments done with radioactive beams produced by RIBRAS were performed using only the first solenoid and chamber-2. In the following, we describe the features that are common to all measurements. The detection system consists of several surface barrier $\Delta E - E$ Si telescopes, with thin (20–25 μm) ΔE detectors, followed by E detectors of 300, 500 or 1000 μm. The secondary targets vary, ranging from light targets, such as ^{9}Be, ^{12}C, or ^{27}Al, to heavier, such as ^{51}V, ^{58}Ni, and ^{120}Sn. However, in all experiments, we alternated runs with the target of interest and a gold target to monitor the secondary beam intensity and to provide an absolute normalization of the cross sections. The scattering of these radioactive projectiles on gold, at the energies and angles we performed experiments, is pure Rutherford.

The elastic scattering cross section in the center-of-mass frame, for the system of interest, can be determined by the expression below:

$$\sigma_{\rm c.m.}(\theta) = \frac{N_c}{N_c^{\rm Au}} \frac{N_b^{\rm Au}}{N_b} \frac{N_t^{\rm Au}}{N_t} \frac{J}{J^{\rm Au}} \sigma_{\rm c.m.}^{\rm Au}(\theta), \qquad (1)$$

where N_c is the area of the peak of interest, J is the Jacobian, a factor of transformation from the laboratory to the center of mass system, N_b is the total number of beam particles during the run, N_t is the surface density of the target of interest in number of atoms/cm^2, $N_c^{\rm Au}$, $J^{\rm Au}$, $N_b^{\rm Au}$, $N_t^{\rm Au}$ are the corresponding numbers with the gold target. This expression has the advantage of being independent of the detector solid angle. The ratio $\frac{N_b^{\rm Au}}{N_b}$ is taken as the ratio of the accumulated charge of the primary beam, measured with the integrator during the runs with gold and the target of interest, and supposes that the production efficiency

did not change with time. Usually, we perform runs with the gold target before and after every run with the target of interest in order to monitor the production rate during the entire experiment.

The elastic scattering experiments described in detail in the following sect. 4 were performed using only the first solenoid. In chamber-2, we have many contaminant beams accompanying the beam of interest. However, elastic scattering is by far the most probable process and it can be identified easily and measured even in the presence of contaminant beams. Moreover, in some experiments, we are able to use the contaminant beams to measure their elastic scattering cross sections also.

To compensate the low intensity of the radioactive beams, we use quite large (10–20 msr) solid angle Si telescopes. In this case, the geometrical mean detection angle is not a good representation in the forward angle region, since the Rutherford cross section on the gold target, for instance, has a very rapid variation with angle, and the effective mean angle has to be weighted by the cross section. The effective detection solid angles and the mean detection angles are obtained from a Monte Carlo simulation [31], which takes into account the collimator in front of the detectors, the secondary beam spot size, the angular divergence of the secondary beam, and the angular distribution at forward angles in the detector, which modifies the average detection angles. The angular resolution (standard deviation) is between 2 and 2.7°, depending on the energy and the colliding system. This error is usually small compared to our angular step and was not indicated in the figures, where we present the angular distributions of the elastic scattering differential cross sections.

A similar effect occurs for the energy loss in the target. Due to the low secondary beam intensity, we normally use thick targets, of the order of a few mg/cm^2 and as a consequence, the energy loss in the target can reach several MeV. Then, the measured cross section is, in fact, the result of an average in energy of the cross sections at each point along the trajectory of the particles inside the target. We have shown in [32] that for the case of pure Rutherford scattering in a thick target, there is an effective energy, which exactly reproduces the average cross section, and corresponds to the geometric mean of the energies before (E_0) and after (E_1) the target, given by: $E_{\rm eq} = \sqrt{E_0 E_1}$. In many applications, where the target is not too thick and the energy loss in the target is relatively small ($\leq 5\%$ of the average energy) this value is very close to the energy in the center of the target, the difference between them being $\leq 0.05\%$. We have calculated the difference for thicker targets [33]; it is, respectively, about 0.6 and 2.5% when the energy losses are about 20 and 40% of the average energy. In these cases (fig. 18) the geometric mean has to be used. The uncertainty of the effective energy can be assumed to be very similar to the uncertainty of the incident energy of the secondary beam, presented in table 1, which already takes into account the energy loss in a gold target.

With the present intensities of our secondary beams, measurements of excitation functions with small energy steps would be very time consuming. However, in the "thick-target method", one can obtain the entire excitation function in one measurement, using a thick secondary target. This method is currently used mainly in inverse kinematics, with reactions between heavier radioactive beams on light proton (p), deuteron (d), or ^{4}He(α) targets. The light targets can be gaseous, liquid, or even solid, refrigerated by cryogenic means, to increase their thickness. In our experiments, we used solid plastic targets of polyethylene foils, $[CH_2]_n$, which are rich in protons.

If the composite system, projectile + target, formed during the collision, presents resonances, they should be populated, from the beam energy down to zero energy, while the radioactive projectile is slowing down in the thick $[CH_2]_n$ polyethylene target. Whenever a resonance is populated, a larger number of ejectiles (p, d, or α) are produced and detected in the Si telescopes located at forward angles, producing a peak in the ejectile (p, d, or α) spectrum. Thus, the energy spectrum of the ejectiles represents the excitation function of the reaction, and peaks in the energy spectrum correspond to resonances in the excitation function.

The main advantage of this method, in the case of light ejectiles (p, d, or α), is the good energy resolution of the excitation function. The energy uncertainty is much smaller than, and practically does not depend on, the energy resolution of the incident beam. This is due to the fact that beam particles with slightly different energies can populate the same resonance at slightly different locations in the target, but the ejectiles emitted arrive at the detector with practically the same energy, due to their small energy loss in the target.

The measurement of the elastic scattering on a proton target in inverse kinematics is more difficult than elastic scattering on a heavier target in normal kinematics (sect. 4), for several reasons: i) in inverse kinematics the recoiling protons are detected and they have lower energy than the contaminant proton beam; ii) the protons lose less energy in the detectors and are more difficult to be detected with good energy resolution than the scattered radioactive nuclei; iii) the low-energy protons stop in the ΔE Si detector and cannot be detected in the telescope, limiting the excitation function at low energies. Thus, measurements of proton elastic scattering in inverse kinematics has to be performed with pure radioactive ion beams. As described in sect. 2.4, the purification of the secondary beam can be achieved using the two solenoids and a degrader foil at the crossover point between them. Recently, a large scattering chamber-3 was installed after the second solenoid and it is in use since 2011.

In the case of the "thick-target method", the cross section calculation has to take into account the energy variation of the projectile in the thick target. The Jacobian is energy dependent in the case of reactions with $Q \neq 0$. The number of target nuclei per unit area, interacting with the projectile during its slowing down is not constant but varies with the projectile energy due to the fact that the energy loss per unit distance varies with the energy. Thus, the differential cross section in the center-of-mass frame is

calculated using

$$\frac{\mathrm{d}\sigma}{\mathrm{d}\Omega}(E,\theta)_{\mathrm{c.m.}} = \frac{NJ\frac{\mathrm{d}E}{\mathrm{d}x}}{\Delta\Omega N_{\mathrm{inc}}\Delta E(^8\mathrm{Li})}\,, \tag{2}$$

where N is the total number of ejectiles detected with energy corresponding to the interval E and $E + \Delta E$, $\Delta\Omega$ is the solid angle of the detector considered, N_{inc} is the number of radioactive secondary ions incident on the secondary target, J is the Jacobian, and $\frac{\mathrm{d}E}{\mathrm{d}x}$ is energy loss per unit distance, also called stopping power [33], of the projectile in the thick $[CH_2]_n$ target.

3.3 Theoretical models

3.3.1 Optical model calculations using the São Paulo Optical Potential (SPP)

The elastic scattering angular distributions are usually analyzed and described by optical model calculations. The Woods-Saxon–type complex nuclear potential is well known and has been largely used for many decades. However, the ambiguities in the potential parameters hinder the access to their physics content and relation with the structure of the nuclei. The idea of folding potentials, which take into account the nucleon distribution in the interacting nuclei was introduced by Feshbach [34]. Their application in data analysis has increased in importance to describe reactions between heavy ions with the contributions of Satchler and Love [35]. More recently, the so-called São Paulo Potential (SPP) [36,37] was proposed by a group of researchers at IFUSP. It is a double-folding nuclear potential which includes the Pauli principle between nucleons by a non-local term and uses densities from experiment (electron scattering) or from Dirac-Hartree-Bogoliubov (HDB) model [38] theoretical calculations. The imaginary part and the real part of this nuclear potential have the same form factor and, for stable systems, it does not have any free parameters. However, for exotic nuclei with anomalies in their geometry, the SPP allows the variation of the normalization of the real and imaginary parts, respectively, N_R and N_I and the diffuseness a of the nuclear density of the projectile. At energies well above the Coulomb barrier the typical values of N_R, N_I and a, which give a good description of most stable nuclear systems are, respectively, 1.0, 0.78 and 0.56 fm [36–38].

3.3.2 Continuum Discretized Coupled Channels (CDCC) calculations

The description of scattering induced by exotic weakly bound nuclei can be improved by the explicit inclusion of the effect of coupling to the continuum. In most cases, the coupling between the elastic and the projectile breakup channel is very important and has to be explicitly taken into account to describe the experimental elastic scattering angular distributions. The effect of the coupling to the breakup states can be described within the framework of the Continuum Discretized Coupled Channels calculations (CDCC) [39]. CDCC has been applied to a number of cases in recent years, first for the three-body problem [40–44] where the projectile is considered as a core plus a valence particle, and more recently, to the four-body problem [45–47].

In a simplified notation, the problem can be reduced to a set of coupled equations:

$$\left[\frac{\mathrm{d}^2}{\mathrm{d}r^2} - \frac{l(l+1)}{r^2} - \frac{2\mu}{\hbar^2}U_{\alpha,\alpha} + k_\alpha^2\right]\chi_\alpha = \frac{2\mu}{\hbar^2}\sum_{\alpha\neq\alpha'}U_{\alpha,\alpha'}\chi_{\alpha'}, \tag{3}$$

where α represents the elastic incoming channel and α' the breakup channels; χ is the wave function of the relative motion between projectile and target. The coupling interaction U is written as the sum of the interaction between each fragment of the projectile with the target, folded with the internal projectile wave function: in the case of a ^{6}He projectile, it can be written as

$$U_{\alpha,\alpha'} = \langle\phi_{\alpha'}(^6\mathrm{He})|U_{n-T} + U_{n-T} + U_{^4\mathrm{He}-T}|\phi_\alpha(^6\mathrm{He})\rangle, \tag{4}$$

where ϕ_α are the internal ^{6}He wave functions and U_{n-T} and $U_{^4\mathrm{He}-T}$ represent the total potential (Coulomb + complex nuclear) for neutron-target and ^{4}He- target respectively. It is to be noted that, in this description, the forces between the target and different particles of the projectile provide a mechanism to excite the projectile from the ground state to continuum states. In addition, the interactions U_{n-T} and $U_{^4\mathrm{He}-T}$ are empirical optical potentials which should contain the effect of all couplings between the projectile fragments and the target. In general, they are fitted on elastic scattering data between a neutron and the target $(n-T)$ and ^{4}He particles and the target $(^4\mathrm{He}-T)$.

A difficulty arises from the fact that the exact continuum wave functions $(\phi_{\alpha'}(^6\mathrm{He}))$, calculated at a single energy, are not square normalizable. One way to overcome this problem is to replace the continuum by a finite set of normalizable states, each one obtained as an average in energy of the wave functions within a certain energy range which is called a "bin". The continuum is then substituted by a set of discrete states, each one normalizable, truncated at a maximum excitation energy. The "bin" width and the maximum excitation energy are empirically determined by imposing the convergence of the cross sections. The coupling interaction inside eq. (4) is expanded in multipoles and the inclusion of internal states with different orbital angular momenta is necessary to describe the projectile excitations. A truncation in the angular momentum space is also required but, in most cases, a few states of low angular momenta $l = 0 - 4$ are sufficient to obtain convergence of the cross sections.

In the three-body model, the ^{6}He structure is simplified to an alpha-particle core plus a di-neutron, which means that the neutron pair is treated as a single particle bound to the alpha core by 0.973 MeV. In an application of the three-body model to $^6\mathrm{He} + ^{209}\mathrm{Bi}$ scattering [42], it was found that 3b-CDCC was unable to reproduce the angular

distributions between 50 and 100°. More recently, an improved 3b-CDCC model was proposed by A.M. Moro [48] which greatly improved the situation. Moro *et al.* demonstrated that the use of a different separation energy for ^{6}He, 1.6 MeV instead of 0.973 MeV, provided results closer to the four-body calculations. Several applications presented in the next sections will make use of this modified three-body model as well as the full four-body calculations [49].

The CDCC framework, described above, takes into account only the breakup of the weakly bound projectile, not of the target. The same formula could be applied to the breakup of the target since, in the center-of-mass system, there is no distinction between projectile and target. However, a simultaneous description of both, projectile and target breakup is not available yet.

4 Scattering on targets with A between 9 and 120

4.1 Elastic scattering of ^{6}He on a ^{120}Sn target

Angular distributions of $^6\mathrm{He} + {}^{120}\mathrm{Sn}$ elastic scattering were measured at four energies, $E_{\mathrm{lab}} = 17.4$, 18.0, 19.8, and 20.5 MeV [23]. These were the beam energies in the center of the 3.8 mg/cm^2 enriched ^{120}Sn (98.3%) target. The energy loss in the target was about 0.8 MeV, and the effective energies calculated as geometric mean (see sect. 3.2) were, respectively, 17.39, 17.99, 19.78 and 20.48 MeV, thus very close to the energies in the center of the target. The uncertainty of the energies is about 4%, mainly due to the uncertainty in the incident ^{6}He energy (see table 1). The Coulomb barrier, $V_{\mathrm{CB}}(\mathrm{lab}) = 13.4$ MeV, was calculated using the São Paulo Potential (SPP). The 10^4–10^5 pps ^{6}He secondary beam was produced in the RIBRAS system via the $^9\mathrm{Be}(^7\mathrm{Li}, ^6\mathrm{He})^{10}\mathrm{B}$ production reaction. The ^{7}Li primary beam with intensity of about 300 nAe was delivered at laboratory energies between 24–26 MeV. Four $E(1000\,\mu\mathrm{m}) - \Delta E(20\,\mu\mathrm{m})$ telescopes formed by surface barrier silicon detectors were used to detect and identify the particles emerging from the reaction target. The experiment was performed in chamber-2.

In this experiment, the ^{6}He secondary beam was selected by the first solenoid only. In fig. 10, we present two-dimensional identification spectra obtained with ^{120}Sn and ^{197}Au targets. The spectrum with the gold target (of 3.0 mg/cm^2 thickness) shows the main beam contaminants at this location, $^7\mathrm{Li}^{2+}$, α-particles, and lighter particles such as tritons, deuterons, and protons, that were produced in reactions between the primary beam and the primary target. In fact, at backward angles, a few counts have been observed in the α-particle line at energies slightly below the energy of the ^{6}He elastic scattering peak. Those counts, as will be discussed later, probably come from the Coulomb breakup of ^{6}He in the Coulomb field of the gold target and, despite their very low intensity, they were included in the area of the ^{6}He elastic peak before using it for normalization.

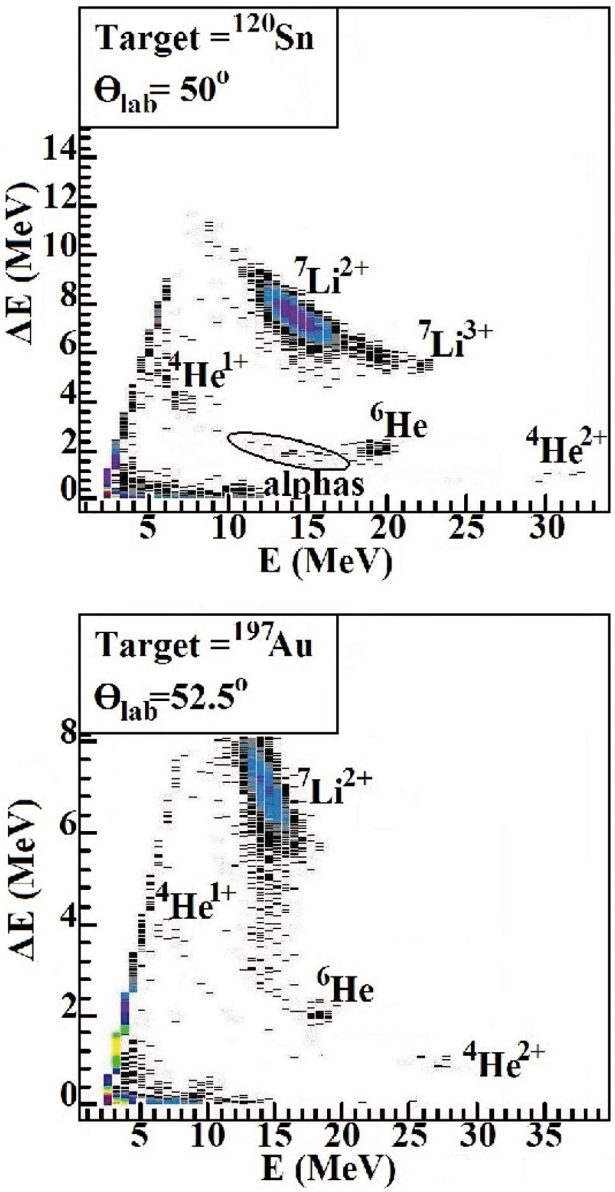

Fig. 10. $E - \Delta E$ identification spectra of the secondary beams scattered on ^{120}Sn and ^{197}Au targets. Taken from ref. [23].

The angular distributions correspond to the angular dependence of the ratio of the elastic scattering differential cross section at a certain angle θ by the Rutherford differential cross section at the same angle, represented by σ/σ_R. They are presented in fig. 11 together with optical model, 3-body (3b), and 4-body (4b) Continuum Discretized Coupled Channels (CDCC) calculations [49], which reproduce the data at the four energies [23]. All three calculations give similar results and the details are discussed below.

We performed optical model fits of the data using a Woods-Saxon shape complex potential. Initially, the four angular distributions were analyzed simultaneously using a single set of potential parameters. This procedure can be justified by the relatively small energy interval of the mea-

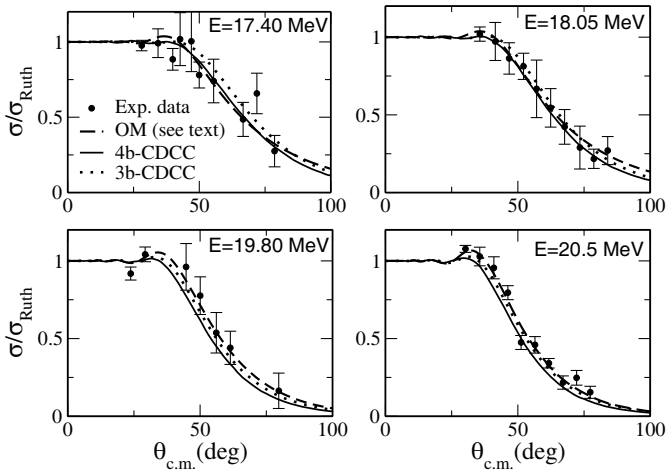

Fig. 11. Angular distributions of the ^{6}He $+^{120}$ Sn elastic scattering. The dashed line is the result of optical model calculations The dotted line is a 3b-CDCC calculation and the solid line is the result of a 4b-CDCC calculation. Taken from ref. [23].

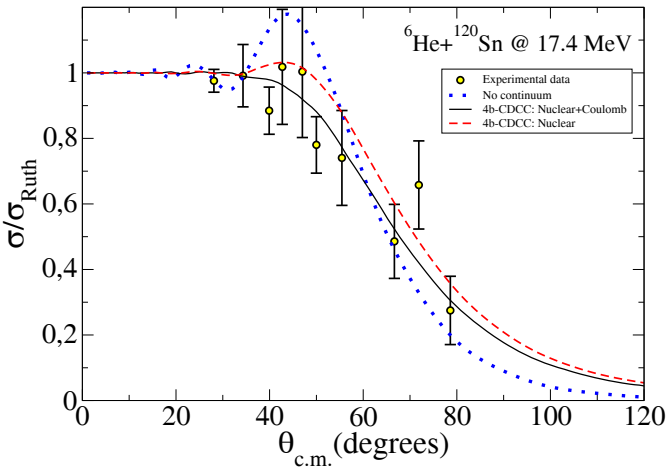

Fig. 12. Comparison between 4b-CDCC and the no-coupling calculations [49]. Blue dotted line is the result of calculations without any coupling to the continuum, red dashed line is 4b-CDCC calculation without Coulomb breakup and the black solid line is the 4b-CDCC with Nuclear + Coulomb breakup. Taken from ref. [23].

surements and the small number of points in each angular distribution. The global Woods-Saxon parameters obtained are: $V_0 = 216.3\,\mathrm{MeV}$, $r_{0r} = 0.90\,\mathrm{fm}$, $a_r = 0.90\,\mathrm{fm}$, $W = 12.42\,\mathrm{MeV}$, $r_{0_i} = 1.42\,\mathrm{fm}$, $a_i = 0.75\,\mathrm{fm}$, where $R = r_0(A_p^{1/3} + A_t^{1/3})$. In a second step, we started the search from the above parameters and let V, r_{0r}, and the imaginary strength W vary freely for each energy. The fits are shown in fig. 11 by dashed lines. Details of these calculations can be found in reference [23]. The large imaginary radius and diffuseness indicate the need for a long-range absorptive term in the interaction potential. A remarkable feature of the best optical potentials [23] is that the imaginary part (W) decreases with increasing energy while the real part (V) increases. This behaviour is still in agreement with the dispersion relation [50, 51], since the increase of V is related to an opposite effect (decrease) in W. A similar behaviour has been previously reported [52,53] in the analysis of weakly bound systems, and is known as the breakup threshold anomaly (BTA). This kind of phenomena will be discussed in more detail in sect. 5.1.

As a complementary approach, we performed three-body and four-body CDCC calculations [49]. The results are presented in fig. 11 as the dotted (3b) and solid (4b) lines. The effect of the coupling with the projectile breakup channel can be better observed in fig. 12 where we compare the no-coupling with the full 4b-CDCC calculation [23]. The no-coupling curve (blue dotted line) corresponds to a calculation using only the ground state part of the coupling potential, see eqs. (3) and (4). This can be considered as an optical model calculation using the bare potential of the CDCC $U_{\alpha,\alpha}$ with $\alpha = gs$. The effect of the breakup is displayed in red dashed (nuclear only) and black solid (nuclear + Coulomb) curves. The red dashed line corresponds to a CDCC calculation considering only the effect of nuclear breakup. The Coulomb potential is removed from the off-diagonal coupling potentials and, consequently no Coulomb breakup is taken into account. The black solid curve corresponds to the full calculation (Coulomb + nuclear). One sees that the effect of the Coulomb breakup is to remove flux from the forward angles region where the Fresnel peak appears and also from the intermediate angles region. This effect is similar to that observed in the past for heavy stable nuclei in systems where the target Coulomb excitation is a reaction channel strongly coupled to the elastic scattering [54]. Coulomb excitation is a process that has a long-range form factor, which also affects mainly the large partial waves, introducing a long-range absorptive component in the polarization potential in a way very similar to Coulomb breakup.

4.2 Elastic scattering of ^{6}He, ^{8}Li and ^{4}He on a ^{51}V target

The first experiment, realized at RIBRAS in February 2004 [55], consisted in the elastic scattering angular distribution measurement of 23.0 and 15.4 MeV ^{6}He and 26.0 MeV ^{8}Li on a $1.9\,\mathrm{mg/cm^2}$ ^{51}V target. These were beam energies in the center of the target and were very close to the effective energies, calculated by the geometric mean, 22.98, 15.39, and 25.99 MeV, respectively. The energy uncertainties are about 4% for the ^{6}He beam and 2% for the ^{8}Li beams, mainly due to the uncertainty in the incident energy of the secondary beams (see table 1). The Coulomb barriers, respectively, $V_{\mathrm{CB}}(\mathrm{lab}) = 7.4\,\mathrm{MeV}$, for the ^{6}He beam, 11.5 MeV for ^{8}Li, and 8.1 MeV for ^{4}He secondary beams on ^{51}V, were calculated using the São Paulo potential (SPP). Thus, the energies were 2 to 3 times the Coulomb barrier. The ^{8}Li secondary beam was produced by the ^{9}Be(^{7}Li, ^{8}Li)^{8}Be reaction and was accompanied by a strong contaminant ^{4}He beam, of the same magnetic rigidity which was also focused by the first solenoid at the center of the chamber-2. The detection system consisted of a $\Delta E(22\,\mu\mathrm{m})$-$E_1(150\,\mu\mathrm{m})$-$E_2(150\,\mu\mathrm{m})$ telescope, formed by three surface barrier silicon detectors.

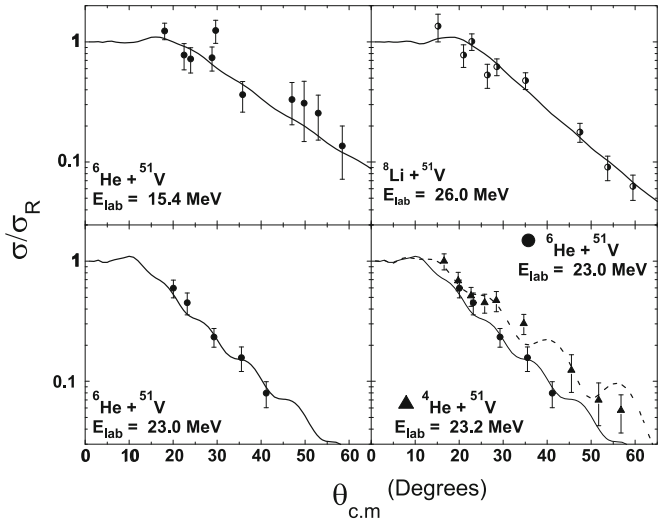

Fig. 13. Angular distributions of the elastic scattering of ^{6}He, ^{8}Li and ^{4}He on ^{51}V target. The solid lines are optical model calculations using the SPP potential [55]. For details about the potential parameters N_I and a, see text.

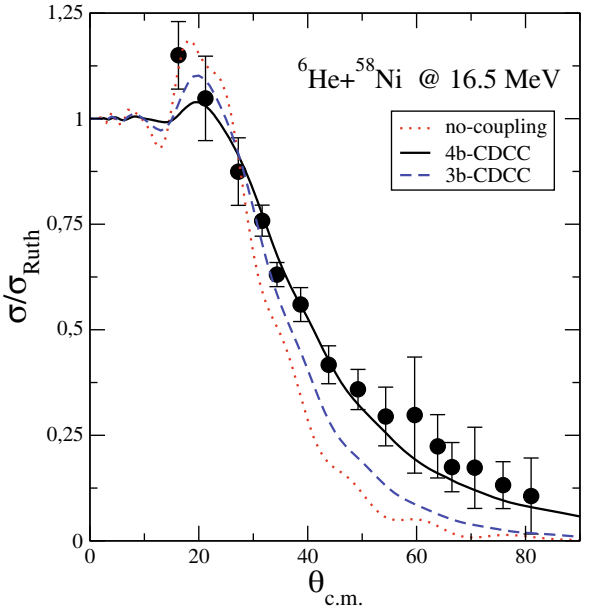

Fig. 14. Angular distribution of $^6\mathrm{He} + {}^{58}\mathrm{Ni}$ elastic scattering. The experimental angular distribution is compared to calculations: red dotted curve is without coupling to the continuum, blue dashed curve is 3b-CDCC calculation and the black solid line is the 4b-CDCC. Taken from ref. [20].

The secondary beam intensities were measured by using the known Rutherford scattering of the secondary beams on a gold target of 5.1 mg/cm^2 thickness.

The angular distributions are shown in fig. 13 and they are compared with optical model calculations using the São Paulo Potential (SPP) [36,37], where the normalization of the imaginary part N_I and the diffuseness, a, of the projectile were adjusted to reproduce the data [55]. The best fit values are $N_I = 1.4(4)$ and $a = 0.67(3)$ fm for $^6\mathrm{He} + {}^{51}\mathrm{V}$ at 23.0 and 15.4 MeV, to be compared to 0.78 and 0.56 fm, respectively, for typical, strongly bound, stable nuclei. As the energies are well above the Coulomb barrier, the disagreement with typical, high energy values of N_I and a, is probably not due to the dispersion relation effects, such as the threshold anomaly [50], described in more detail in sect. 5. To better describe the data, the diffuseness of the density of the two-neutron halo projectile ^{6}He had to be increased from 0.56 to 0.67 fm. Moreover, the normalization of the imaginary part, which describes the absorption, taking away flux from the elastic channel into reaction channels, had to be increased from 0.78 to 1.4, which means that the potential with ^{6}He is more absorptive, than with tightly bound, stable projectiles.

On the other hand, for $^8\mathrm{Li} + {}^{51}\mathrm{V}$ at 26.0 MeV, the best fit values are $N_I = 1.7(7)$ and $a = 0.49(4)$ fm. The value of the diffuseness was even smaller, but still close to the "normal" value of 0.56 fm, indicating agreement with the fact that ^{8}Li has no neutron halo, but it is weakly bound and, thus, has a larger absorption, yielding a large value for N_I.

Due to the presence of a strong contaminant beam of ^{4}He with 23.2 MeV energy in the center of the ^{51}V target, the elastic scattering of $^4\mathrm{He} + {}^{51}\mathrm{V}$ was also measured and analyzed. For the tightly bound ^{4}He projectile we used its well-known density distribution, determined by electron scattering on ^{4}He [56]. The density distribution of ^{4}He has a much smaller diffuseness, $a = 0.3$ fm, than the value adopted for most stable nuclear systems, $a = 0.56$ fm. For the ^{51}V target, its diffuseness was determined by the best fit, to be $a = 0.59(5)$ fm, close to the usual value for stable nuclei. However, the N_I parameter presented a much lower best fit value of 0.45(15), instead of 0.78, indicating that the potential for ^{4}He is less absorptive than for other stable nuclei.

Figure 13 (lower right) also displays the differences between the two systems $^4\mathrm{He} + {}^{51}\mathrm{V}$ and $^6\mathrm{He} + {}^{51}\mathrm{V}$ at comparable energies. It is clear that the exotic $^6\mathrm{He} + {}^{51}\mathrm{V}$ system presents a much steeper angular distribution in comparison with the stable $^4\mathrm{He} + {}^{51}\mathrm{V}$, due to the stronger absorption in the former.

4.3 Elastic scattering of ^{6}He on a ^{58}Ni target

Elastic scattering angular distributions for the intermediate mass $^6\mathrm{He} + {}^{58}\mathrm{Ni}$ system have been measured at three energies $E_{\mathrm{lab}}(^6\mathrm{He}) = 12.2$, 16.5, and 21.7 MeV. These are beam energies in the center of the 2.2 mg/cm^2 thick, enriched ^{58}Ni target and are very close to the effective energies calculated as the geometric mean (12.192, 16.496, 21.698 MeV). The energy losses in the target were between 0.5 and 0.8 MeV. The uncertainty in the energies is about 4%. The Coulomb barrier in the laboratory frame, calculated for this system by the SPP, is 8.8 MeV. Four $E(1000\,\mu\mathrm{m}) - \Delta E(20\,\mu\mathrm{m})$ telescopes formed by surface barrier silicon detectors were used to detect and identify the particles emerging from the reaction target. The experiment was performed in chamber-2. [20].

In fig. 14, we present the 16.5 MeV angular distribution compared with no-continuum CDCC, three, and four-body CDCC calculations [49] considering projectile breakup [20].

The agreement between the four-body CDCC and the experimental data is remarkable. The no-continuum calculation (red dotted line) corresponds to a CDCC calculation without taking into account the coupling to the breakup states as described in more detail in sect. 4.1 and clearly does not reproduce the features of the experimental angular distribution. It predicts a pronounced Fresnel diffraction peak at forward angles and, in addition, underestimates the cross sections at backward angles. The three-body CDCC calculation (blue dashed line) improves the situation by reproducing the behaviour at forward angles. However, it is the four-body calculation which really reproduces the data in the entire angular range of the measurements. It is important to mention that there are no adjustable parameters in these calculations. All of the optical potentials have been obtained from known potentials from the literature for the $\alpha + {}^{58}$Ni and $n + {}^{58}$Ni systems at the appropriate energies. Consequently, these calculations are predictions [20].

In general, CDCC is a very complex calculation which does not give much room for physical insights. The bare potential is the part of the optical potential, that contains the effects of all couplings, except for the projectile breakup channel. The effect of the projectile breakup on the elastic scattering should be described either by a complete CDCC calculation or by a polarization potential which, once added to the bare potential, should exactly reproduce the results of the complete CDCC calculation. However, the exact polarization potential is, in general, a very complicated, non-local quantity and cannot be obtained without approximations. Nevertheless, since we are able to perform such a CDCC calculation, it is possible to define a local equivalent polarization potential $V_{\rm pol}(r)$ from the inversion of eq. (3) [49]. This local equivalent polarization potential will be obtained numerically from the CDCC results, and will be energy and angular momentum dependent. The trivially local equivalent polarization potential is the local equivalent polarization potential averaged over the angular momenta. This trivially equivalent local polarization potential, once added to the bare potential, should reproduce, approximately, the exact CDCC calculation and would display the main effects due to the coupling to the breakup channel.

In fig. 15, we present the trivially equivalent local polarization potential ($V_{\rm pol}$) obtained from the CDCC calculations for ^{6}He + ^{58}Ni at 16.5 MeV. We note the presence of the long-range absorptive imaginary component and a repulsive real polarization potential centered near the surface of the nucleus. These characteristics seem to be general for the polarization potentials from the ^{6}He breakup and have been observed in ^{6}He + ^{120}Sn and in the lighter system ^{6}He + ^{9}Be [12]. In fig. 15, we plot also the bare potential ($V_{\rm bare}$), which is given by $U_{\alpha,\alpha'}$ from eq. (4), with $\alpha = \alpha' =$ ground state, and the $V_{\rm bare} + V_{\rm pol}$. We see that the effect of the coupling is to enhance the absorption and, at the same time, to increase the repulsion in the region of the Coulomb barrier due to the repulsive real component. This kind of effect on the Coulomb barrier would reduce the fusion cross section at these energies.

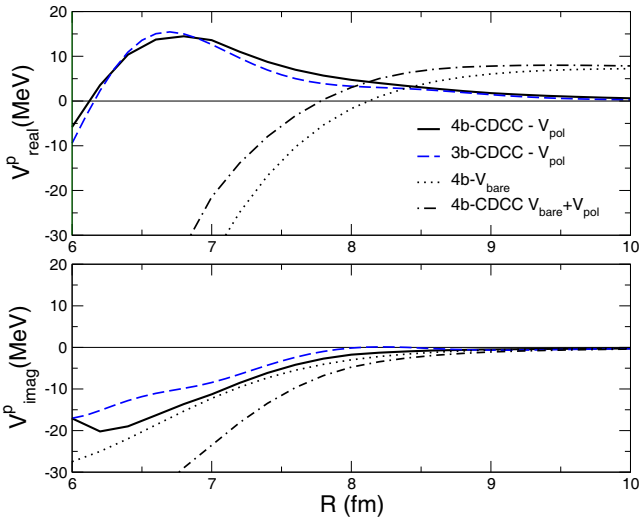

Fig. 15. Polarization potentials for the projectile breakup process in the ^{6}He + ^{58}Ni elastic scattering at 16.5 MeV. The dotted line is the bare potential in the 4-body calculation, the blue dashed and the black solid lines are, respectively, the polarization potentials in the 3b-CDCC and 4b-CDCC. The dash-dotted line is the sum of the bare potential and the 4b-CDCC polarization potential.

4.4 The ^{6}He + ^{27}Al and ^{6}He + ^{9}Be systems

From the studies of ^{6}He scattering on heavy ($A = 120$) and intermediate mass ($A = 51$ and 58) targets presented above, one concludes that the projectile breakup is a very important process to be considered if one wishes to reproduce all of the features of the experimental data. For such systems and energies, the breakup process can occur either in the long range Coulomb or in the short range nuclear field and seems to be strongly coupled to the elastic channel. The extension of the measurements to light targets is interesting since it could, in principle, provide information on the interplay between Coulomb and nuclear breakup [44].

For light targets, the relative importance of the Coulomb field decreases considerably and, the nuclear breakup turns out to be the most important process. Using the ^{6}He secondary beam produced by the RIBRAS system, we have investigated the elastic scattering for two light systems ^{6}He + ^{27}Al [28] and ^{6}He + ^{9}Be [12]. In fig. 16, we present four angular distributions of the ^{6}He + ^{27}Al scattering at 9.5, 11.0, 12.0, and 13.4 MeV laboratory energies, which were the energies in the center of the 7.2 mg/cm^2 thick ^{27}Al target. The energy loss in the target is about 3 MeV. The effective energies, respectively 9.31, 10.87, 11.89 and 13.32 MeV, were calculated by the geometric mean. The energy uncertainty is about 400 keV and it is larger than the differences between the effective energies and the energies used in the calculations. The Coulomb barrier, $V_{\rm CB}$(lab) = 4.9 MeV, was calculated using the SPP.

The experimental angular distributions are compared with the results of optical model calculations using the São

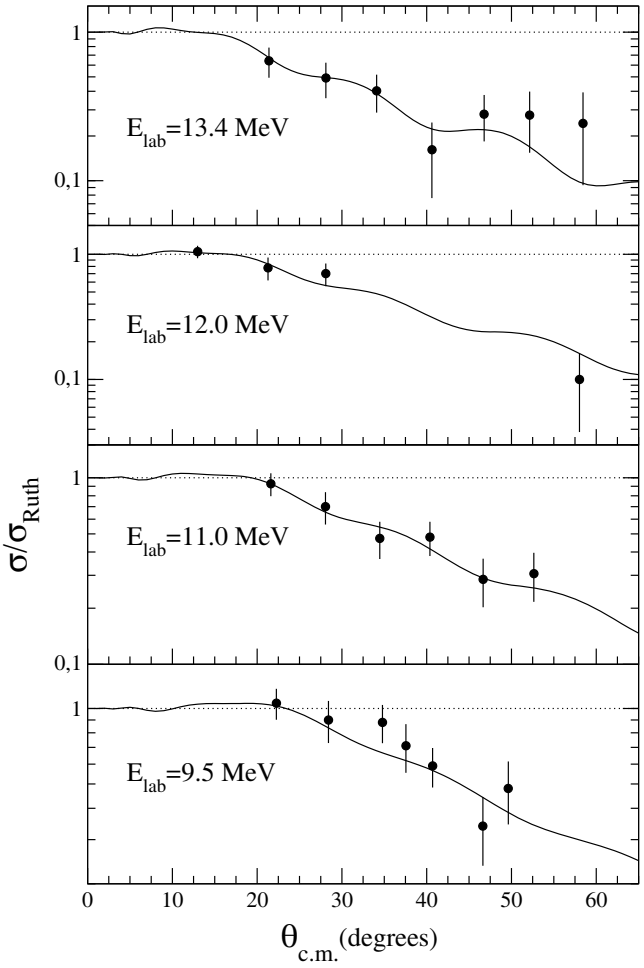

Fig. 16. The elastic scattering angular distributions measured for the ^{6}He + ^{27}Al system together with best fits obtained with the São Paulo potential (SPP). Taken from ref. [28].

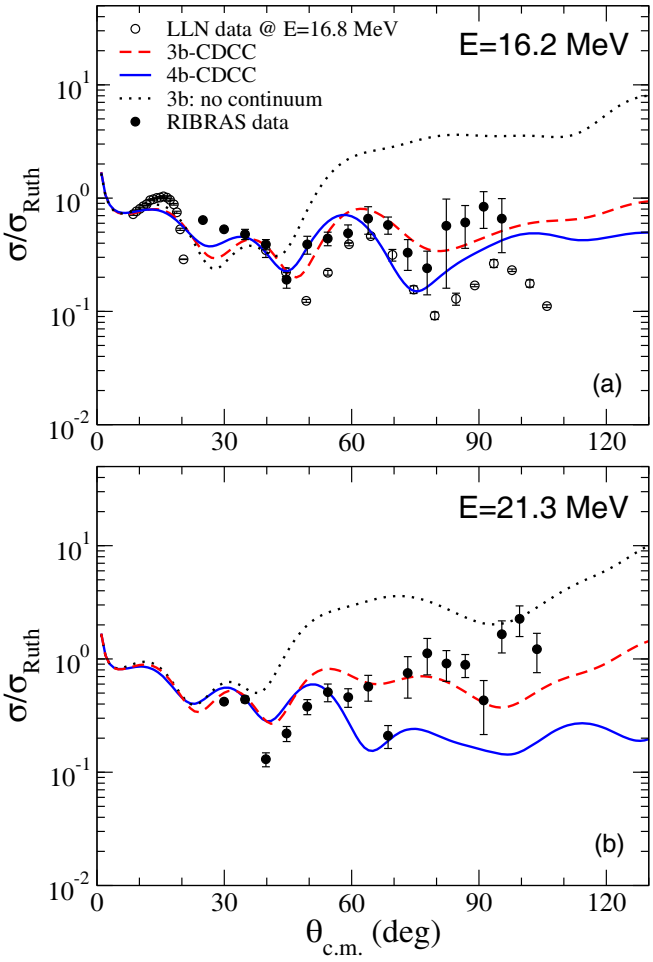

Fig. 17. Angular distributions of the ^{6}He + ^{9}Be elastic scattering. The black dots are experimental results measured at RIBRAS and the circles are data obtained at 16.8 MeV at the Cyclotron Resource Center of Louvain-la-Neuve (CRC-LLN) [57]. The black dotted line is the result of a calculation with no-coupling to the continuum, the red dashed line is the 3b-CDCC calculation, and the blue solid line is the 4b-CDCC result. Taken from ref. [12].

Paulo Potential (SPP) [36,37], where the normalization of the imaginary part N_I and the diffuseness, a, of the projectile are adjusted to reproduce the data [28]. The best fit values are $N_I = 0.8(5)$, $0.8(4)$, $0.6(4)$ and $0.7(5)$ for the energies of 9.5, 11, 12 and 13.4 MeV, respectively. All values are in agreement with the typical value of $N_I = 0.78$ within the uncertainty. The same holds for the diffuseness, with a best fit value of 0.56(2) fm for all energies. When this projectile diffuseness is deconvoluted from the intrinsic matter distribution of the nucleon, one obtains the diffuseness of the point nucleon matter distribution for ^{6}He of 0.52(2) fm. This value is much larger than the similar diffuseness of ^{4}He, which is 0.3 fm, deduced in a similar manner [58, 59]. This value is in agreement with other experimental evidence [58–60]. However, this diffuseness, measured in the elastic scattering on a light target ($A = 27$), is smaller than that obtained with a heavier target ($A = 51$).

In fig. 17, we present experimental data for the elastic scattering of ^{6}He + ^{9}Be at two energies, 16.2 and 21.3 MeV. These were beam energies in the center of the 1.9 mg/cm^2 ^{9}Be target. The energy losses in the target were respectively 0.8 and 0.65 MeV and thus the effective energies (geometric mean) (see sect. 3.2) were very close to the energies in the center of the target, similarly to that verified in the previous systems. The uncertainty of the energies was about 4%. The Coulomb barrier, $V_{\rm CB}$(lab) = 2.2 MeV, was calculated using the São Paulo potential (SPP). Here we see, for the first time, strong oscillations in the experimental angular distributions. Such oscillations are of a different nature than those observed in heavy and intermediate mass systems. For the ^{6}He + ^{9}Be data, the energies are well above the Coulomb barrier, about 6-8 times. It means that, for those data, the Coulomb interaction is not important and we observe a diffraction pattern of Fraunhofer type rather than the Fresnel type observed so far for heavier systems. The data are compared with the result of three and four-body CDCC calculations. The agreement is reasonable. Effects of the angular resolution of the detectors and of the angular divergence of the beam are important in this al-

most symmetric system, due to the kinematic transformations between c.m and laboratory angles. To take into account these effects, all the calculations have been averaged over the angular aperture of the data. It has a considerable effect on the amplitude of the oscillations, which are damped.

4.5 Elastic scattering of ^{7}Be on ^{51}V and ^{27}Al targets

Some beams other than ^{6}He and ^{8}Li were also produced by the RIBRAS system. Among them, ^{7}Be and ^{10}Be were also used for elastic scattering measurements. ^{7}Be is an unstable, proton-rich nucleus with a half-life of 53.24 days, decaying to its mirror nucleus ^{7}Li by electron capture. Its separation energy to α+^{3}He is 1.58 MeV, which characterizes it as a weakly bound nucleus. Despite its low separation energy when compared to the mirror ^{7}Li ($E_{\rm sep} = 2.46$ MeV for $\alpha + t$), it is not sufficiently small to allow the formation of a proton halo, as presumably occurs in the case of ^{8}B ($E_{\rm sep} = 0.137$ MeV).

We measured the elastic scattering of ^{7}Be on an intermediate mass target, $^{7}\mathrm{Be} + {}^{51}\mathrm{V}$ [26,62] and on a lighter target, $^{7}\mathrm{Be} + {}^{27}\mathrm{Al}$ [32,61]. In the $^{7}\mathrm{Be} + {}^{51}\mathrm{V}$ case, one angular distribution was measured at $E_{\rm lab} = 26.0$ MeV and this was the beam energy in the middle of the target, but since the ^{51}V target was not too thick (1.9 mg/cm^2), this value is close to the effective energy. The Coulomb barrier, $V_{\rm CB}({\rm lab}) = 15.66$ MeV, is lower than the energy used in this experiment. The angular distribution was fitted by optical model calculation with the São Paulo Potential [36]. In this analysis, the diffuseness of the projectile mass distribution, a, and the normalization of the imaginary part of the potential, N_I, were varied to obtain the best fit to the data [26,62]. The best fit diffuseness of ^{7}Be was 0.55 fm, which is very close to the typical result used for stable nuclei, 0.56 fm. It should be mentioned that the density radius, obtained from electron scattering measurements of stable neighbour isotopes, or from HDB calculations, is not varied in these OM fits. The best fit normalization factor was $N_I = 1.4$, with a large uncertainty, since equivalent fits yielded N_I ranging between 1 and 2. Again, the diffuseness close to the usual value is compatible with the fact that ^{7}Be has no halo (as we observed also for ^{8}Li), but the high N_I value indicates that the potential describing the system's interaction is more absorptive, due to the weak binding energy of ^{7}Be.

For $^{7}\mathrm{Be} + {}^{27}\mathrm{Al}$ [32,61], four angular distributions were measured at 10.0, 13.8, 15.2 and 15.4 MeV. These energies are effective energies, calculated as geometric mean, between the incident and outgoing energies (see sect. 3.2). The Coulomb barrier, $V_{\rm CB}({\rm lab}) = 10.5$ MeV, is close to the energies used in this experiment. The angular distributions are presented in fig. 18 and refer to quasi-elastic data since the energy resolution is not sufficient to separate the ^{7}Be first excited state at 0.43 MeV. They have been analyzed by the optical model using the São Paulo Potential (SPP), whose normalizations of the real and imaginary potentials were varied to obtain the best fit to the data. Again the uncertainties of N_I and N_R were very large,

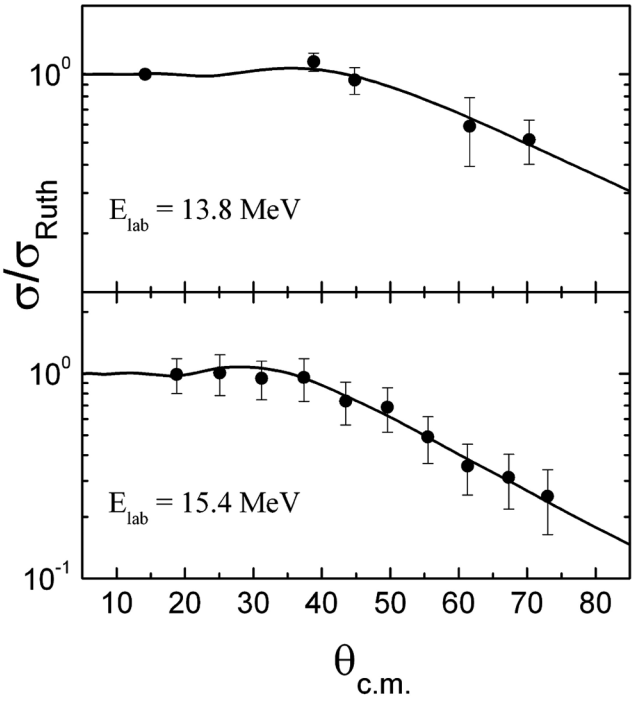

Fig. 18. Quasi-elastic angular distributions of $^{7}\mathrm{Be} + {}^{27}\mathrm{Al}$ [61]. The solid lines are optical model calculations, using the SP potential. Taken from ref. [32].

with an average value of ≈ 1. The total reaction cross sections, however, could be determined with a quite good precision, and their discussion is given in sect. 7.1.4.

4.6 The elastic scattering of ^{7}Be, ^{9}Be, and ^{10}Be on the ^{nat}C target

Another series of elastic scattering measurements have been performed with radioactive projectiles, ^{7}Be and ^{10}Be, on a target of natural carbon (^{nat}C) [21]. The carbon target has been chosen to investigate possible nuclear effects, which are expected to be more important for a lower Z target, rather than the Coulomb effects expected to be dominant for higher Z (heavier-mass) targets.

Elastic scattering angular distributions of beryllium isotopes, ^{7}Be, ^{9}Be, and ^{10}Be, on a natural carbon target of 1 mg/cm^2 were measured at $E_{\rm lab} = 18.8$ MeV, 26.0 MeV, and 23.2 MeV, respectively [21]. These are beam energies in the center of the target and were very close to the effective energies, given by the geometric mean (18.78, 25.98 and 23.18 MeV). The energy uncertainties are about 4%. The Coulomb barriers, respectively, $V_{\rm CB}({\rm lab}) = 6.5$ MeV, for the ^{7}Be beam, 6.9 MeV for ^{9}Be, and 7.2 MeV for ^{10}Be secondary beams on carbon, were calculated using the São Paulo potential (SPP). These angular distributions are displayed in figs. 19, 20 and 21. The angular distributions for the $^{7}\mathrm{Be} + {}^{nat}\mathrm{C}$ were measured in part at the Nuclear Structure Laboratory of the University of Notre Dame with the TwinSol device [9] by Barioni *et al.* [63] and in part at São Paulo with RIBRAS [21] (see fig. 19). Also, angular distributions were measured for the ^{10}Be

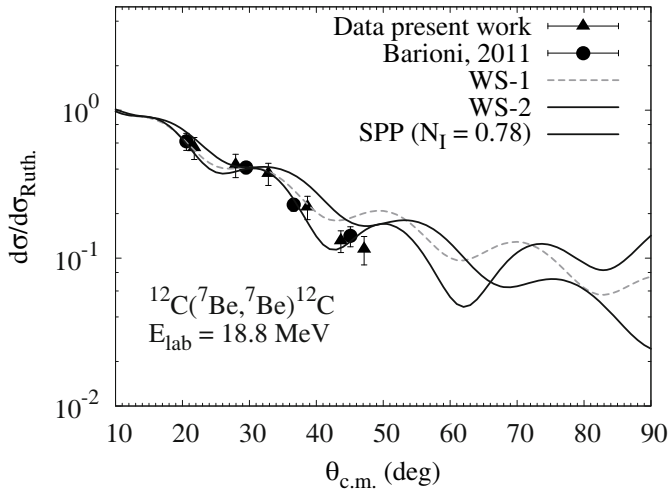

Fig. 19. The differential cross sections for the elastic scattering ^{nat}C(^{7}Be, ^{7}Be)^{nat}C at 25.8 MeV incident laboratory energy. The data represented by triangles were measured at RIBRAS [21] and those by dots at Notre Dame by Barioni 2011 [63]. The curves are optical-model calculations. Taken from ref. [21].

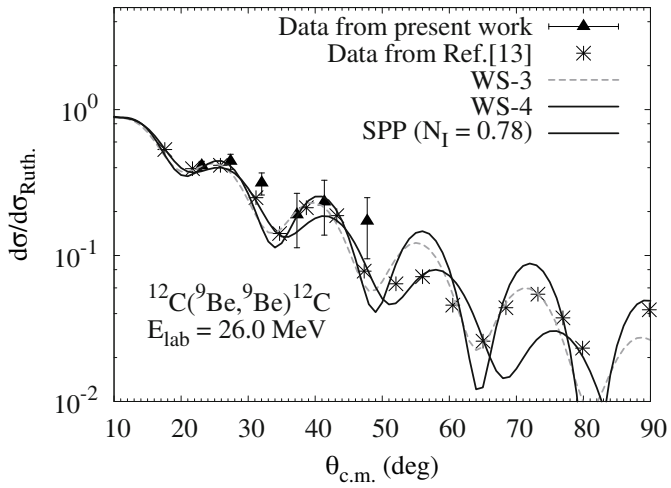

Fig. 20. The differential cross sections for the elastic scattering ^{nat}C(^{9}Be, ^{9}Be)^{nat}C at 18.8 MeV incident laboratory energy. The curves are optical-model calculations. Taken from ref. [21].

radioactive ion beam together with the contaminant ^{9}Be ions, which was simultaneously produced by the RIBRAS system.

These angular distributions were analyzed with a conventional optical model (OM) in terms of both the volume type Woods-Saxon (WS) and the São Paulo double-folding (SPP) potentials [36,37]. We applied the normalization factor $N_I = 0.78$ for the imaginary part of the double-folding São Paulo Potential. The WS optical potentials used in our calculations were obtained from other work with projectiles of similar mass on a carbon target. The parameters of all potentials are listed in table 2. The results of this optical-model analysis can be seen in figs. 19, 20 and 21. As can be observed, the WS potentials considered here give a good description of the data

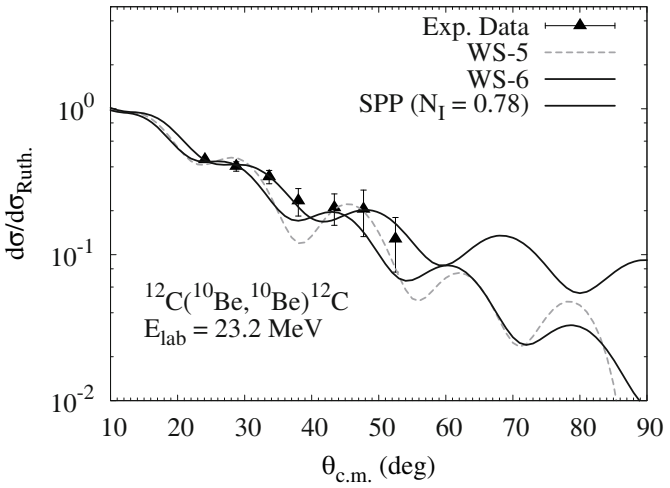

Fig. 21. The differential cross sections for the elastic scattering ^{nat}C(^{10}Be, ^{10}Be)^{nat}C at 12.3 MeV incident laboratory energy. The curves are optical-model calculations. Taken from ref. [21].

at forward angles. The SPP, which can be considered as a bare potential, also reproduces quite well the absolute normalization for the forward angle cross sections, which is of some interest considering that this folding-model potential has no free parameters. The São Paulo Potential, however, fails to reproduce the backward angle range of the angular distribution. An improvement of the description of the data could be obtained by adjusting the normalizations of the real and imaginary part of the potential, N_R and N_I, respectively, and this is a clear indication of the importance of other reaction channels.

We have also performed a detailed analysis with coupled-channel calculations for each of the present systems and the details of these calculations can be found in ref. [21]. We have performed CDCC calculations [49] for elastic scattering induced by the weakly bound ^{7}Be and ^{9}Be isotopes. From this analysis, we concluded that the Coulomb and nuclear breakup effects are not relevant for these light projectiles on light target systems. For ^{10}Be, which is a tightly bound nucleus, we performed a coupled channel calculation coupling the first two bound states, which involve quadrupole transitions. By only including a short-range imaginary bare potential (to account for the fusion channel) and the coupling to the bound states, it was possible to describe the cross sections for the ^{10}Be + ^{12}C angular distribution.

4.7 The ^{8}Li + ^{12}C experiment: Elastic and transfer reactions

The low-energy RIBs produced by the RIBRAS system are very reliable for investigating not only elastic scattering but also transfer reactions. We have measured angular distributions for both elastic and proton transfer reactions for the ^{8}Li + ^{12}C system at 23.9 MeV laboratory energy, which was the energy in the center of the natural carbon target [25]. The effective energy, 23.89 MeV, was very close

Table 2. Optical potential parameters used in the calculations of the elastic scattering of $^{7,9,10}\mathrm{Be} + {}^{nat}\mathrm{C}$. Radii are given by $R_x = r_x \times (A_P^{1/3} + A_T^{1/3})$. The total reaction cross section is σ_R and its units are mb. The depths are in MeV, radii and diffuseness in fm.

Potential	V	r_V	a_V	W	r_W	a_W	r_C	σ_R	Reference
WS-1	33.69	1.00	0.92	6.53	1.56	0.49	0.65	1278	from $^{9}\mathrm{Be} + {}^{12}\mathrm{C}$ [64]
WS-2	94.18	1.26	0.60	59.84	1.48	0.20	1.48	1224	(fitting)
WS-3	60.00	1.18	0.60	32.60	1.18	0.60	0.63	1428	from $^{9}\mathrm{Be} + {}^{12}\mathrm{C}$ [65]
WS-4	100.00	1.23	0.48	17.00	1.30	0.26	1.45	1327	from $^{11}\mathrm{B} + {}^{12}\mathrm{C}$ [66]
WS-5	100.00	1.15	0.50	10.00	1.30	0.22	1.40	1182	from $^{10}\mathrm{B} + {}^{12}\mathrm{C}$ [66]
WS-6	32.35	0.89	0.85	5.77	1.37	0.36	0.62	1004	(fitting)

to the energy in the center of the target. The energy uncertainty was about 2%. The scattered and reaction product particles ^{8}Li and ^{9}Be were easily separated by the $\Delta E - E$ silicon detector telescopes.

The Coulomb barrier for this system is 4.9 MeV calculated with the São Paulo Potential (SPP). The measured angular distribution for the elastic scattering was analyzed with the standard procedure of optical-model (OM) calculations using volume-type Woods-Saxon (WS) and double-folding nuclear potentials (plus Coulomb potentials due to uniformly charged spheres). The results of this calculation can be seen in more detail in ref. [25]. Although CDCC calculations have been performed for this system [49], no significant influence of the breakup channel on the elastic scattering was observed.

In addition to the elastic scattering, we have also measured the angular distribution for the proton transfer reaction, $^{12}\mathrm{C}(^{8}\mathrm{Li}, {}^{9}\mathrm{Be})^{11}\mathrm{B}$, which has a positive Q_{gg} value = 0.931 MeV. The differential cross sections for this transfer process are very small (in the range of 0.1 to 1.0 mb/sr), which made the measurements and analysis difficult due to the limited secondary beam intensity. Cross sections were obtained only for the most forward angles between 20 to 35°. This proton transfer angular distribution has been analyzed in terms of a FR-DWBA (finite-range distorted-wave Born approximation) calculation. For the entrance ($^{8}\mathrm{Li} + {}^{12}\mathrm{C}$) and exit ($^{9}\mathrm{Be} + {}^{11}\mathrm{B}$) channels, we used the double-folding São Paulo potential. The bound-state wave functions were generated with Woods-Saxon potentials and geometric parameters $r = 1.25$ fm and $a = 0.65$ fm, with the depths of the potentials adjusted to give the correct separation energies. By comparing this calculation with the experimental angular distribution, we could extract the spectroscopic factor for the bound system $\langle {}^{9}\mathrm{Be}_{gs} | {}^{8}\mathrm{Li}_{gs} + p \rangle$. More details about this analysis can be obtained in ref. [25].

The spectroscopic factor obtained for the $\langle {}^{9}\mathrm{Be}_{gs} | {}^{8}\mathrm{Li}_{gs} + p \rangle$ bound system from the present analysis is compared with other experimental values in table 3. Our result agrees within the experimental error with the values obtained from the $(\mathrm{d}, {}^{3}\mathrm{He})$ [67], (t, α) [68], and $^{9}\mathrm{Be}(^{8}\mathrm{Li}, {}^{9}\mathrm{Be})^{8}\mathrm{Li}$ reactions [69], but it is twice that obtained from the (d, n) reaction [70]. This difference could be, in part, due to the use of different potential models.

Table 3. Spectroscopic factors C^2S of $\langle {}^{9}\mathrm{Be}_{gs} | {}^{8}\mathrm{Li}_{gs} + p \rangle$.

	SM calc. ($\mathrm{p}_{3/2} + \mathrm{p}_{1/2}$)	Other exp. values	This work ($\mathrm{p}_{3/2} + \mathrm{p}_{1/2}$)
$J^\pi = 3/2^-$	1.00[a], 0.87[b]	0.64[c]	1.22(28)
		1.00[d]	
		1.059[e]	
		1.67(31)[f]	

[a] SM calculation from Cohen and Kurath [72].
[b] SM calculation with WBT interaction (OXBASH) [73].
[c] $\mathrm{d}(^{8}\mathrm{Li}, \mathrm{n})^{9}\mathrm{Be}$ reaction at 40 MeV [70].
[d] $^{9}\mathrm{Be}(\mathrm{d}, {}^{3}\mathrm{He})^{8}\mathrm{Li}$ reaction at 52 MeV [67].
[e] $^{9}\mathrm{Be}(\mathrm{t}, \alpha)^{8}\mathrm{Li}$ reaction at 15 MeV [68].
[f] $^{9}\mathrm{Be}(^{8}\mathrm{Li}, {}^{9}\mathrm{Be})^{8}\mathrm{Li}$ reaction at 27 MeV [69].

A consistent systematic investigation on neutron spectroscopic factors has been performed by M.B. Tsang *et al.* [71] and a similar systematic investigation for proton spectroscopic factors would be most welcome. We also compared our results with the value predicted by the shell-model (SM) calculation by Cohen and Kurath [72] and, also, a new calculation using the WBT interaction with code OXBASH [73]. Our values agree better with the SM calculation by Cohen and Kurath, $C^2S_{\mathrm{calc}}(^{9}\mathrm{Be}_{gs}) = 1.00$, than with the new one, $C^2S_{\mathrm{calc}}(^{9}\mathrm{Be}_{gs}) = 0.87$.

5 Threshold Anomaly (TA) and Breakup Threshold Anomaly (BTA)

In addition to the elastic scattering angular distributions, the analysis of the energy dependence of the experimental data is also very important and can provide information on the dynamics of the couplings. The classical example is the well-known threshold anomaly (TA), which occurs in the scattering of stable heavy systems, such as $^{16}\mathrm{O} + {}^{208}\mathrm{Pb}$, at energies in the vicinity of the Coulomb barrier [50]. In this case, the number of open reaction channels is large at energies above the Coulomb barrier and decreases strongly for energies below the barrier. As a consequence, the imaginary part of the optical potential is strongly reduced when

the incident energies decrease below the Coulomb barrier. This sharp reduction in the imaginary potential induces, via the dispersion relation, an enhancement in the real part of the optical potential, which becomes more attractive at the top of the Coulomb barrier.

More recently, an interesting phenomenon has been reported, related to the behaviour of the energy dependence of the optical potential for weakly bound systems, such as ^{6,7}Li on medium mass targets, at energies around and below the Coulomb barrier [52,53]. Instead of a decrease, an increase in the imaginary potential has been observed for energies lower than the Coulomb barrier. Consequently, the effect on the real part of the potential is the appearance of a repulsive component, in opposition to the behaviour of the usual threshold anomaly. The explanation for this behaviour comes from the fact that, for weakly bound systems, the number of open reaction channels, such as breakup and neutron transfers, could be still large, even at very low energies. Due to the low binding energies in these systems, the coupling to reaction channels in the continuum would lead to the appearance of repulsive real polarization potentials that could explain the behaviour observed in the real potential. This new kind of anomaly was called the breakup threshold anomaly (BTA) and has been reported in several systems since then.

5.1 An optical model analysis of the ^{6}He + ^{120}Sn data

Here we present an optical model analysis performed for the ^{6}He + ^{120}Sn data of sect. 4.1 which seems to give an alternative explanation for the BTA phenomena. As we pointed out (see sect. 4.1), the effective energies are practically the same as the energies in the center of the target that were used in the calculations. The energy uncertainties (standard deviation σ) are $\sim$ 300 keV, thus smaller than the energy steps between the data. In this optical model analysis [74], a double folding potential, using a density-dependent nucleon-nucleon interaction, was used for the real potential, $V(r) = \lambda V_F(r/w)$. Two parameters $\lambda \approx 1.1$–1.4 and $w \approx 1.00(5)$ were adjusted to fit the experimental data. λ is a normalization and w modifies slightly the slope of the potential. The nuclear densities of ^{120}Sn and ^{4}He, used in the double folding calculation, have been derived from experimental measurements of charge-density distributions [56].

The imaginary potential was parametrized by a Woods-Saxon volume shape plus a surface (derivative of Woods-Saxon) term,

$$W = W_v \times f_v(r) + W_s \times f_s(r), \tag{5}$$

where

$$f_v(r) = \frac{1}{1 + \exp(\frac{r-R}{a})}, \tag{6}$$

and $f_s(r) = -4a\mathrm{d}f_v(r)/\mathrm{d}r$ with $R_S = r_s(A_1^{1/3} + A_2^{1/3})$ and $a = 0.7$ fm is the diffuseness, which was fixed during the analysis. The volume term should describe fusion and was, in fact, neglected in the analysis, $W_v = 0$. The surface term describes the effect of the peripheral, direct reactions. The remaining parameters W_s and r_s were adjusted to reproduce the data. For a reduction in the number of parameters, a systematic investigation of the volume integral of the potentials from a previous analysis was used [75,76], which imposes relations between the parameters W_s and r_s in order to reproduce the systematic behaviour of the volume integrals. The results are presented in fig. 22 for the ^{6}He + ^{120}Sn system and the parameters are in table 4. The volume integrals $J_{R,I}$ of the potentials are also presented in table 4.

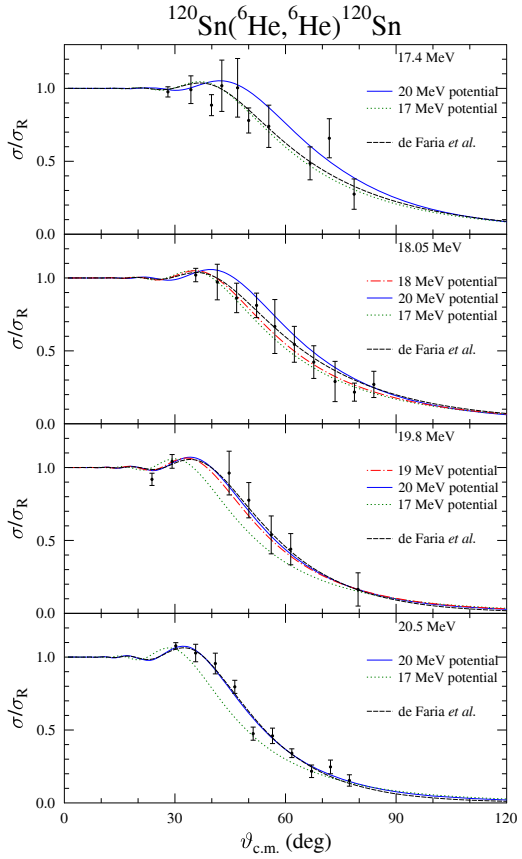

Fig. 22. ^{6}He + ^{120}Sn optical model analysis. Details of the energy-dependent potentials are in the text. The black solid line is the result of calculations using the optical potentials referred in sect. 4.1. Taken from ref. [74].

The agreement with the data is excellent. We also plot in the figure the results that would be obtained, for each energy, using the potential of the other three energies to display the relevance of the energy dependence. An interesting effect was observed (fig. 23) in the energy dependence of the position of the imaginary surface term r_s for the ^{6}He + ^{120}Sn system. The parameter r_s moves outwards for decreasing energies. This indicates that the direct processes are becoming more and more peripheral as the energy decreases as if they were expelled by the repulsive effective barrier. However, the total reaction cross section and the volume integral of the imaginary potential decrease for lower energies, as expected for the usual threshold anomaly. Then, we find from this analysis, that

Table 4. Parameters of the potentials of ^{6}He + ^{120}Sn elastic scattering in fig. 22. J_R and J_I are the volume integral, respectively, of the real and imaginary potentials.

$E_{\rm lab}$ (MeV)	λ	w	J_R (MeV fm^3)	$R_{R,\rm rms}$ (fm)	J_I (MeV fm^3)	$R_{I,\rm rms}$ (fm)	W_S (MeV)	r_s (fm)	a (fm)	$\sigma_{\rm reac}$ (mb)
17.4	1.207	0.95	339.0	5.477	75.6	9.320	19.2	1.315	0.7	1479
18.0	1.210	0.95	339.9	5.477	78.0	9.074	21.0	1.277	0.7	1503
19.8	1.219	0.95	342.4	5.477	83.8	8.415	26.6	1.174	0.7	1538
20.5	1.222	0.95	343.2	5.477	85.9	8.153	29.3	1.133	0.7	1546

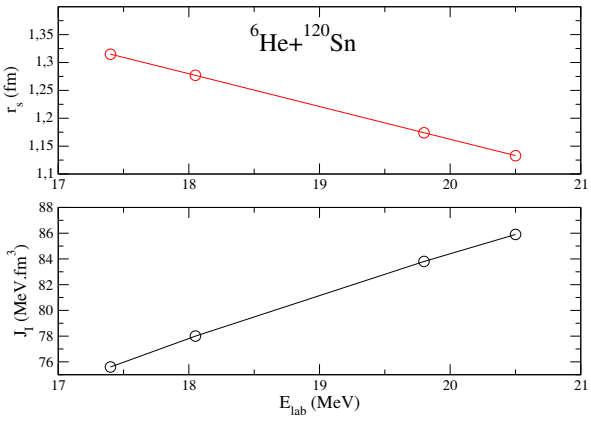

Fig. 23. Evolution of the position of the imaginary surface term as a function of the energy (top). The same for the volume integral of the imaginary potential (botom) [74].

the introduction of a surface component in the imaginary potential, whose position (R_S) and intensity (W_S) is left free to vary, accounts for the energy dependence of the data without the need for an increase in the imaginary potential for lower energies.

6 Scattering on hydrogen target

6.1 The ^{6}He(p, p)^{6}He elastic scattering excitation function at energies E*(^{7}Li) = 10.4–11.7 MeV

The excitation function measurements of the ^{6}He + p elastic scattering can provide information about states of the compound nucleus ^{7}Li in a region of excitation energies above the proton threshold (9.975 MeV). The first resonance above the threshold is located at 11.24 MeV excitation energy, total width $\Gamma = 265$ keV, and $J^\pi = 3/2^-$ and $T = 3/2$ [77]. This state, which corresponds to the Isobaric Analog State (IAS) of the ^{7}He ground state, was studied recently by the ^{6}He(p,n)^{6}Li reaction [78]. The observation of this state in the elastic scattering is of great interest due to theoretical studies, since an unusual behaviour is expected, with the reduced neutron decay width γ_n larger than the γ_p with $\gamma_n/\gamma_p = 1.4$. In this case, the elastic scattering should be weaker than the neutron decay.

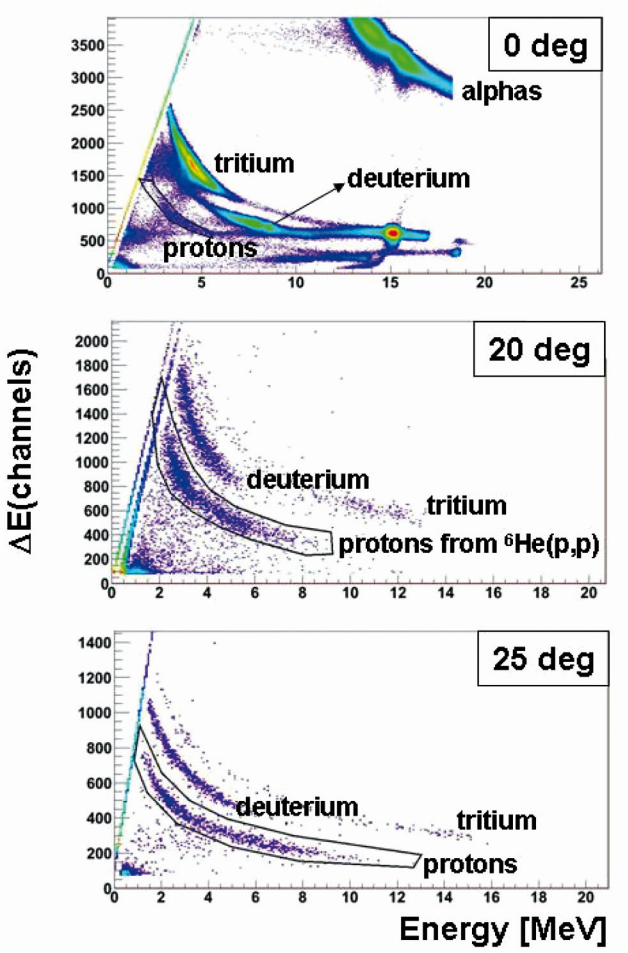

Fig. 24. Two-dimensional identification spectra of particles from the ^{6}He + $[CH_2]_n$ collision. The contours on the figure are indicating the detected protons. Taken from ref. [79].

Preliminary measurements of the elastic scattering excitation function of ^{6}He(p, p)^{6}He [19] were performed in the range $E^*(^7\text{Li}) = 10.4$–11.7 MeV with the ^{6}He beam produced by RIBRAS. This measurement was performed using chamber-3, a degrader in chamber-2, and a purified ^{6}He beam (92%) (instead of 16%, without degrader). The previously described "thick-target method" was used, with a 12 mg/cm^2 $[CH_2]_n$ secondary target, which was thick enough to fully stop the ^{6}He beam of 11.5 MeV energy. Three $\Delta E - E$ Si telescopes were placed at very forward angles (one of them at 0°). In fig. 24 we show bidi-

mensional ($\Delta E - E$) identification spectra of the particles coming from the thick $[CH_2]_n$ target, obtained at 0°, 20°, and 25°. Those angles correspond, respectively, to 180°, 140°, and 130° in the center of mass of the ^{6}He(p, p)^{6}He scattering. We observe the presence of alphas, tritons, deuterons, and protons. The most intense alpha, triton, and deuteron peaks seen in the spectrum at zero degrees are remnant contaminants of the secondary beam. The spectra at 20° and 25° are much cleaner and the region of interest, corresponding to the 11.24 MeV resonance in the proton line, is indicated. A clear peak is observed in the energy spectra at the three angles, corresponding to the correct position and total width of the 11.24 MeV resonance [19,79]. However, R-matrix calculations, considering the two-channels (p, p) and (p, n), do not reproduce the shape and the angular distribution of the peak. The analysis is in progress.

6.2 The ^{8}Li(p, p)^{8}Li elastic scattering excitation function measured between E*(^{9}Be) = 17.5 and 19.0 MeV

The main purpose of this work was to obtain new information on the ^{9}Be structure near the proton threshold (16.888 MeV) through ^{8}Li(p, p)^{8}Li elastic scattering. The ^{9}Be level scheme is well known at low excitation energies [80,81], but the high-energy region still has many uncertainties. The ^{8}Li(p, p)^{8}Li elastic scattering allows the precise determination of several resonance parameters: energies, spins, parities, and proton widths.

The ^{8}Li(p, p)^{8}Li measurement was performed in chamber-3 with the nearly pure (95–99%) ^{8}Li beam on the secondary targets. They were, respectively, a $[CH_2]_n$ polyethylene foil of 7.7 mg/cm^2 thickness and a gold target of 5 mg/cm^2 thickness. The identification spectra measured by the $\Delta E - E$ Si telescope had very good energy resolution and the protons resulting from the ^{8}Li(p, p)^{8}Li reaction were well separated from other light particles. In fig. 25, we can see the two-dimensional identification spectra obtained using the thick $[CH_2]_n$ target.

The presence of contaminant α-particles, as well as deuterons and tritons can also be observed in the identification spectra of fig. 25 despite the purification of the secondary beam. These contaminations did not depend on the target and they could be measured in the runs with the gold target. As a matter of fact, some contaminant protons were also observed in the runs with the gold target and they were subtracted from the spectra measured with the $[CH_2]_n$ target. Measurements with a natural carbon target of 15 mg/cm^2 were also realized and the same background was observed as with the gold target, indicating no contribution due to the carbon content of the polyethylene. The precise normalization of the spectra obtained with different targets is essential before the background subtraction; however, it is not straightforward, since the secondary beam ^{8}Li stops in the thick $[CH_2]_n$ target and it is not detected. These subtractions are responsible mainly for the large error bars of the final excitation function presented in fig. 26.

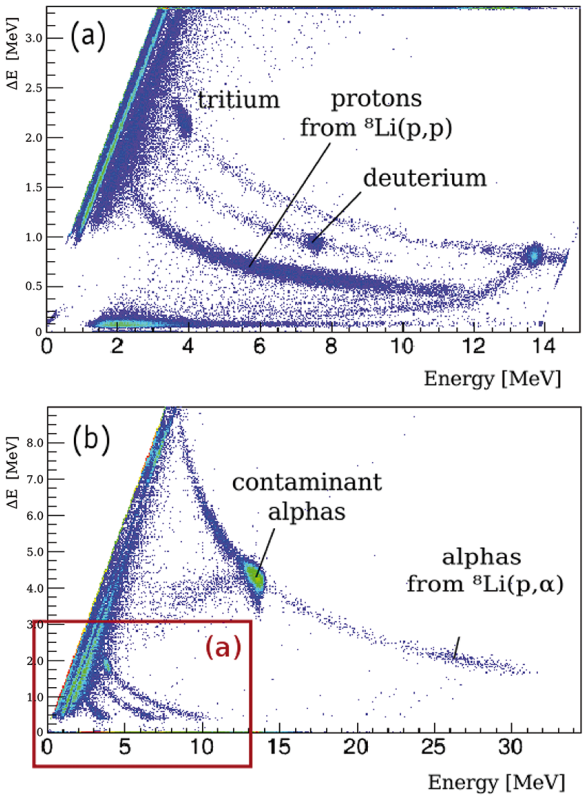

Fig. 25. Two-dimensional identification spectra obtained using a $E - \Delta E$ Si detector telescope at $\Theta_{lab} = 10°$, in the large chamber-3, with the purified ^{8}Li secondary beam focused on a $[CH_2]_n$ target. Spectrum on the top is a zoom of the spectrum on the bottom.

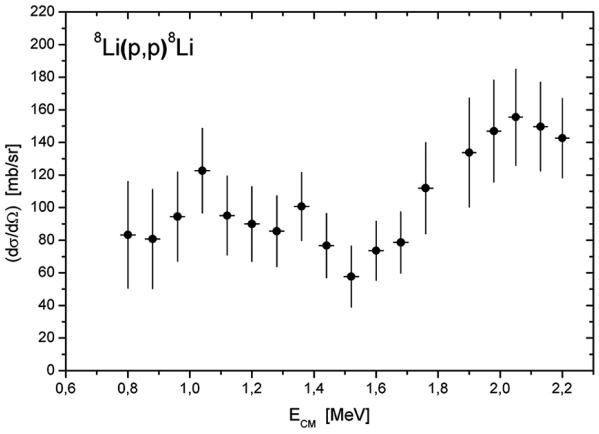

Fig. 26. Elastic scattering excitation function of the ^{8}Li + p system measured at $\Theta_{lab} = 10°$.

The ^{8}Li(p, d)^{7}Li and ^{8}Li(p, α)^{5}He reactions could also be observed in this experiment. The preliminary result of the elastic scattering excitation function of the ^{8}Li + p system is shown in fig. 26. All data are being analyzed and the excitation functions are going to be fitted by R-matrix calculations [82,83].

6.3 The excitation function of the ^{8}Li(p, α)^{5}He reaction

For some reactions with high positive Q-value, the cross section can be measured even in the presence of contaminant beams. One example is the ^{1}H(^{8}Li, α)^{5}He reaction, with $Q = +14.42$ MeV. We have measured the cross section of this reaction at low energies [13]. This measurement was performed using only the first solenoid of the RIBRAS system.

The main purpose of this work was to combine the information from the ^{8}Li(p, α)^{5}He and ^{8}Li(p, p)^{8}Li reactions. Both reactions populate the same high lying resonances in ^{9}Be, with the same entrance channel and different decay channels. In the phenomenological R-matrix theory [82,83], the inputs for each resonance are the spin and parity (J^π), the angular momenta (l), the resonance energy ($E_\circ$), and the partial widths of the incoming channel (γ_p) and the outgoing channel (γ_α). However, in the description of the ^{8}Li(p, p)^{8}Li and ^{8}Li(p, α)^{5}He reactions by the same model, some parameters, such as the spin and parity of the resonance, its energy, and the incoming proton partial width γ_p are the same, thus the measurement of both channels can constrain the parameters strongly. Moreover, a transfer reaction has several advantages: in particular, the isospin of the exit channel limits the population to $T = 1/2$ states in ^{9}Be, and interference with the Coulomb interaction, which is dominant in elastic-scattering experiments, is absent in a transfer reaction.

Some reactions involving ^{8}Li can also play a role in nuclear astrophysics [84]. Specifically, in the inhomogeneous Big-Bang nucleosynthesis, the ^{8}Li(α, n)^{11}B reaction (see ref. [85] and references therein) could be a path to cross the $A = 8$ gap and was investigated by various groups (see, for example, ref. [86] and references therein). More recently, this reaction was quoted as a possible seed for the r-process nucleosynthesis [87] and, for this reason, the role of other reactions involving ^{8}Li could be an important issue. In particular, the ^{8}Li(p, α)^{5}He is important because it not only depletes the ^{8}Li, but it feeds back to low masses, avoiding the production of higher Z nuclei. The ^{8}Li(p, α)^{5}He reaction was previously measured at a single energy $E_{\rm c.m.} = 1.5$ MeV [88]. We have performed this measurement to provide experimental cross sections over a wide range of energy (from $E_{\rm c.m.} = 0.2$ MeV to 2.1 MeV).

In fig. 27, we present the two-dimensional identification spectrum of the scattered ^{8}Li and contaminant beams, measured with a $\Delta E - E$ telescope at 13.5° on a $[CH_2]_n$ reaction target. The spectrum of the measurement with the gold target is presented in fig. 3 in sect. 2.3 and it clearly shows all of the contaminant beams scattered on gold, with ^{4}He being the second most intense ($\sim$ 31%) after the beam of interest ^{8}Li ($\sim$ 66%). Figure 27 shows that, due to its large positive Q-value, the reaction of interest can be clearly observed, with no interference from the contaminants.

In order to obtain a complete excitation function, even in the presence of contaminant peaks, we have made measurements at four incident energies of 13.2(3), 14.5(3), 17.0(4), 19.0(4) MeV. The secondary targets were

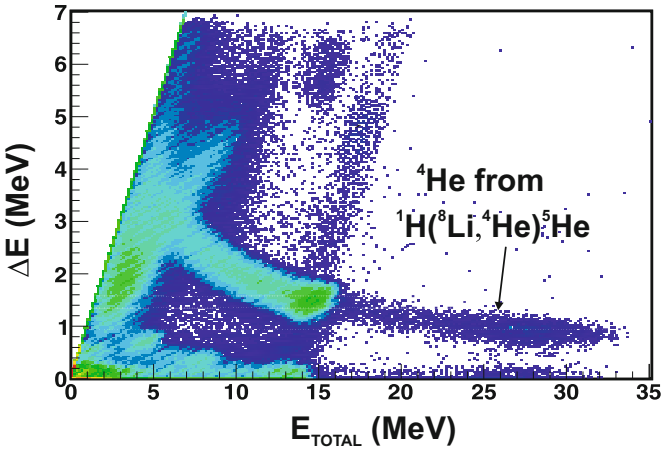

Fig. 27. Two-dimensional identification spectrum obtained in a $E-\Delta E$ Si telescope at $\theta_{\rm lab} = 13.5°$ with ^{8}Li secondary beam at $E_{\rm lab}(^8{\rm Li}) = 19.0$ MeV focused by the first solenoid, on the $[CH_2]_n$ secondary target. Taken from ref. [13].

a $[CH_2]_n$ polyethylene foil 6.8 mg/cm^2 thick and a gold target 5 mg/cm^2 thick used for normalization purposes. Due to the positive Q-value of the reaction (+14.42 MeV), the α particles had high kinetic energy and were detected at forward angles using four $\Delta E(20\,\mu{\rm m}) - E(1000\,\mu{\rm m})$ Si telescopes positioned at four angles. The maximum incident energy in the laboratory frame corresponds to $E_{\rm c.m.} = 2.11$ MeV for the p+ ^{8}Li system, thus all resonances in ^{9}Be below $E_{\rm c.m.} = 2.11$ MeV could be populated while the ^{8}Li projectiles are slowing down in the thick target.

In the ^{8}Li(p, α)^{5}He reaction, the recoiling ^{5}He is unbound and disintegrates into an α-particle and a neutron. Similarly, in the ^{8}Li(p, n)^{8}Be reaction, the ^{8}Be is unbound, breaking into two α-particles. The contribution of these α-particles, as well as the continuous energy distribution of α-particles resulting from the 3-body breakup, were calculated and subtracted from the energy spectra. All details of these calculations can be obtained in the reference of Mendes *et al.* [13].

The results of this experiment [13] are presented in fig. 28 which contains two excitation functions. The one on top represents the measured excitation function of the reaction ^{8}Li(p, α)^{5}He with the R-matrix fit. In the spectrum located on the bottom, we present this same spectrum, with a zoom of the low-energy resonances and their R-matrix fit. These data show evidence of a broad peak near $E_{\rm c.m.} \approx 1.7$ MeV, which can be fitted only by assuming two overlapping resonances at energies 1.69 and 1.76 MeV, which are consistent with known spectroscopic properties of ^{9}Be [77]. The existence of a broad structure near $E_{\rm c.m.} \approx 1.76$ MeV ($E_x = 18.6$ MeV in ^{9}Be) has already been suggested by a previous ^{7}Li(d, α)^{5}He experiment [89], and is consistent with the overlapping states observed in the present experiment.

The astrophysical S-factor and the reaction rate for the ^{8}Li(p, α)^{5}He reaction was calculated from the angle integrated cross section obtained from the R-matrix

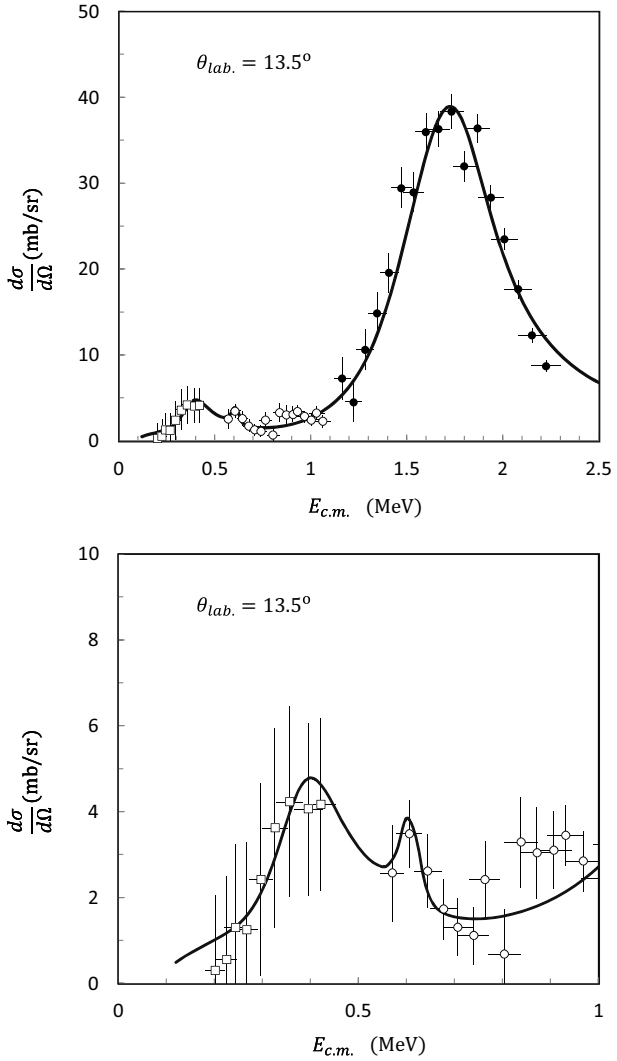

Fig. 28. Top: The ^{8}Li(p, α)^{5}He differential cross sections at $\theta_{\rm lab} = 13.5^\circ$, with the R-matrix fit (solid line.) Bottom: The same reaction, with a zoom on the low-energy resonances and their R-matrix-fit. Taken from ref. [13].

calculation. In fig. 29, we present the ^{8}Li(p, α)^{5}He and ^{8}Li(α, n)^{11}B reaction rates multiplied by the proton X_p and α mass fractions, X_p and X_α, where we take the standard values of Big Bang, *i.e.*, $X_p = 0.75$ and $X_\alpha = 0.25$. This comparison shows that the reaction rate of the (p, α) reaction, which yields the depletion of ^{8}Li, is faster than the (α, n) reaction, which could bridge the $A = 8$ gap.

7 Reaction and breakup cross sections

7.1 Total reaction cross sections comparisons

7.1.1 Comparison of total reaction cross sections of different systems: scaling procedures

The experimental determination of the total reaction cross section is quite cumbersome, since all reaction channels

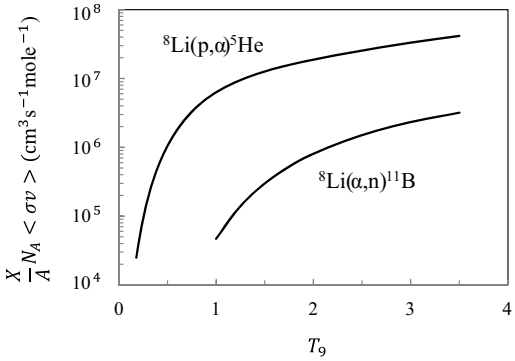

Fig. 29. Left: The ^{8}Li(p, α)^{5}He and ^{8}Li(α, n)^{11}B reaction rates multiplied by the proton and α mass fractions, $X_p = 0.75$ and $X_\alpha = 0.25$. Taken from ref. [13].

and the fusion cross section should be measured and summed up to yield this quantity. The total reaction cross section can be also deduced from elastic scattering angular distributions, using the well-known sum-of-differences method:

$$\sigma_{\rm reac} = 2\pi \int_{\theta_0}^{180} [\sigma_{\rm Ruth}(\theta) - \sigma(\theta)] \sin\theta \, {\rm d}\theta. \qquad (7)$$

This expression is simply the difference between the Rutherford and the experimental elastic differential cross sections, integrated over the whole angular range, except for a small cone around zero degrees, where the Rutherford cross section diverges. θ_0 can be chosen in such way that, for $\theta < \theta_0$, the difference in the argument of the integral is null. However, in practical applications of the above formula, the experimental angular distributions are usually not sufficiently complete and, in order to evaluate the integral, $\sigma(\theta)$ is replaced by a model calculation which should reproduce the data. In this sense, the result is model dependent since the differential cross sections $\sigma(\theta)$ have been obtained from optical model or CDCC calculations and not directly from measurements. Moreover, the experimental angular distributions are, in many cases, not sufficiently precise and complete to decide between different models and provide a precise determination of the total cross section. The use of the parameter-free, double-folding potentials, such as the São Paulo potential, can reduce considerably the ambiguities. Comparing total reaction cross sections for different systems can be an interesting way to investigate the influence or competition of reaction mechanisms, such as breakup, transfer, and fusion. This can be particularly revealing, if these systems have weakly bound or exotic projectiles.

In order to compare total reaction cross sections for systems of different masses and charges at different energies, it is necessary to use a scaling procedure to remove trivial effects due to different sizes and energies with respect to the Coulomb barriers. The interest in the comparison of many systems, after eliminating the above cited trivial features, is to see more subtle differences due to the intrinsic structure of the nuclei (*i.e.* static effects, such as halo structure) or dynamic effects due to couplings be-

tween various reaction channels and the elastic scattering. According to refs. [90] and [91], dynamic effects would be more important in the region near and below the reduced barrier, and static effects would be relevant for all energies.

There are two procedures proposed by [92–95] that have been used in recent years. Here we use both. In the first scaling procedure [92,93] the reduced reaction cross section $\sigma_{\rm red}$ and the reduced energy $E_{\rm red}$ are defined, respectively, in eqs. (8) and (9), below:

$$\sigma_{\rm red} = \sigma_{\rm reac}/({A_p}^{1/3} + {A_t}^{1/3})^2, \tag{8}$$

and

$$E_{\rm red} = E_{\rm c.m.}({A_p}^{1/3} + {A_t}^{1/3})/Z_p Z_t, \tag{9}$$

where Z_p (Z_t) and A_p (A_t) are, respectively, the charge and the mass numbers of the projectile (target) and $\sigma_{\rm reac}$ is the total reaction cross section measured for the system. This procedure accounts for the geometrical effects in the cross section due to the size of the system and a part due to the effect of the Coulomb barrier. It is important to understand how this scaling behaves in the case of weakly bound projectiles. The increase of the reaction cross sections of weakly bound projectiles, due either to a fit of the elastic scattering angular distributions or by explicit consideration of the projectile breakup process in the case of a CDCC calculation, is expressed in $\sigma_{\rm reac}$ and $\sigma_{\rm red}$ and is not removed by the scaling. On the other hand, the possible lowering of the Coulomb barrier due to the increase in the radius of weakly bound projectiles is not washed out by this scaling. However, this scaling does not consider the change in the curvature of the barrier, which certainly affects the fusion cross sections. The role of the barrier curvature on the total reaction cross section is still an open question.

To include the barrier curvature also into the geometrical description, Canto and collaborators introduced the concept of the fusion functions for the systematic study of fusion processes in recent work [94,96]. Inspired by the tunneling concept of the Wong model [97], the dimensionless "fusion function" $F_F(\chi)$ is defined as

$$F_F(\chi) = \frac{2E}{\hbar\omega R_B^2}\sigma_F. \tag{10}$$

It is proportional to the fusion cross section σ_F, and depends on a dimensionless variable χ defined as

$$\chi = \frac{E - V_B}{\hbar\omega}\,, \tag{11}$$

where R_B, V_B, and $\hbar\omega$ are, respectively, the radius, height, and curvature of the Coulomb barrier. They were obtained from a parabolic fit to the barrier, calculated using the SPP + Coulomb potential. When the Wong model [97], which describes fusion as a tunneling process through the Coulomb barrier, is valid, the fusion functions can be described by a "Universal Fusion Function" (UFF), which does not depend on the system and is defined as

$$F_0(\chi) = \ln[1 + e^{2\pi\chi}]. \tag{12}$$

This procedure allows the elimination of all static effects and has been used to compare fusion cross sections of different systems, transforming σ_F into the fusion function $F_F(\chi)$.

Inspired by this new scaling, Shorto *et al.* [95] applied the same concept to total reaction cross sections, defining a total reaction function $F_{TR}(\chi)$, as

$$F_{TR}(\chi) = \frac{2E}{\hbar\omega R_B^2}\sigma_{\rm reac}. \tag{13}$$

The quantity $F_{TR}(\chi)$ is the scaled or reduced total reaction cross section. This second procedure, based on the UFF, works very well for the scaling and comparison of fusion cross sections, since it is based on the concept of tunneling through the fusion barrier. However, an important fraction of the reaction cross section does not come from tunneling but from peripheral, direct processes, such as the inelastic excitations and transfer reactions. Due to this fact, the concept of UFF can be inappropriate for the reaction cross sections and this is still an open debate: which is the best reduction method to apply to total reaction cross sections. In order to contribute to this open question, we applied both procedures to some of our results and, in the following, we compare and discuss the similarities and differences.

7.1.2 Total reaction cross sections on targets with mass number $A \approx 120$

The total reaction cross sections of the ^{6}He + ^{120}Sn system, obtained from the 3b-CDCC, 4b-CDCC, and optical model calculations [23], have been averaged and are presented in table 5. The dispersion between them increases with energy, attaining $\sim$ 15–20% at the highest energy. They are also presented in fig. 30 together with the cross sections for other systems with tightly and weakly bound projectiles on targets with mass number around 120. In the upper part of fig. 30, the first scaling described above by eqs. (8) and (9) was used for several projectiles, among tightly and weakly bound nuclei and including the halo nucleus ^{6}He on heavy targets with mass number $A \sim 120$. In the lower part of fig. 30, the other scaling, based on the total reaction function $F_{TR}(\chi)$ (see eq. (13)) derived from a parabolic Coulomb barrier, was used.

With both procedures, we see that the reduced cross sections follow three trends with increasing magnitude, from tightly bound to weakly bound and exotic projectiles. It can be noted that the reduction based on the "reaction function" does not bring the tightly bound and weakly bound systems together, as was observed in the case of fusion cross sections [94,96]. We interpret this result as a manifestation of the fact that, for systems with doubly magic tightly bound projectiles, such as α-particles or ^{16}O, there are very few reaction channels open. In fact, the Q-values for proton or neutron transfer reactions are very negative in the ^{4}He + ^{120}Sn case. As a consequence, fusion must be the most important reaction channel contributing to the total reaction cross section, with some possible weak

Table 5. Total reaction cross sections for the ^{6}He + ^{120}Sn [23] system obtained from the Optical Model and CDCC calculations. The fourth column is the average between the second and third columns. (See text for more details).

E (MeV)	$\sigma_{\rm reac}^{\rm OM}$ (mb)	$\sigma_{\rm reac}^{\rm CDCC}$ (mb)	$\sigma_{\rm reac}^{av}$ (mb)	$\sigma^{\rm halo}$ (mb)	$\sigma_{\rm fus} = \sigma_{\rm reac}^{av} - \sigma^{\rm halo}$ (mb)	$\sigma_{\rm fus}^{\rm Bass}$ (mb)
17.40	1451	1491	1471	768	703	618
18.05	1445	1592	1519	763	756	703
19.80	1475	1834	1655	739	916	900
20.50	1579	1916	1748	762	986	1065

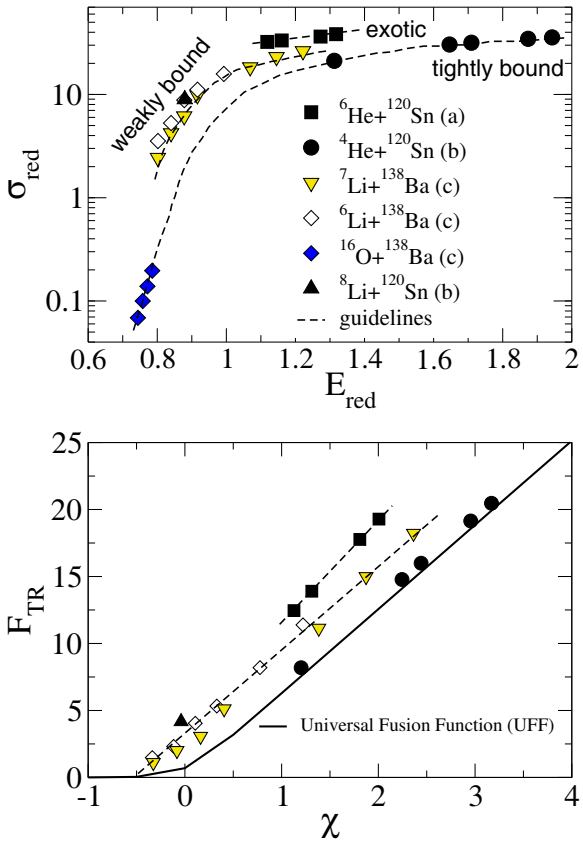

Fig. 30. Top: reduced total reaction cross sections for several systems with target mass numbers around 120 [23]: (a) from ref. [23], (b) from ref. [98], (c) from refs. [99, 100]. The units of $\sigma_{\rm red}$ and $E_{\rm red}$ are, respectively, mb and MeV. Bottom: The total reaction function F_{TR} for the same systems. The solid line is the prediction of UFF, calculated from eq. (12). Taken from ref. [23].

contributions from inelastic excitations of the target. As we go to systems with weakly bound projectiles, such as ^{6,7}Li and ^{9}Be, the situation changes. The binding energies of these projectiles are much smaller, ranging from 1.45 to 2.46 MeV and their cluster structure favors the occurrence of transfer reactions. Finally, for the exotic ^{6}He projectile, the two-neutron separation energy (^{6}He $\rightarrow \alpha + 2$n) is even smaller (0.973 MeV) and, its two-neutron halo favors the occurrence of breakup and neutron transfer reactions, which increase even more the total reaction cross section.

From this picture, we may define the *halo cross section* as

$$\sigma^{\rm halo} = \left[\sigma_{\rm red}^{^6{\rm He}+^{120}{\rm Sn}} - \sigma_{\rm red}^{^4{\rm He}+^{120}{\rm Sn}}\right] \times (6^{1/3} + 120^{1/3})^2. \quad (14)$$

This quantity is the difference between the total reaction (^{6}He breakup + neutron transfers + incomplete fusion + complete fusion) and the complete fusion process (^{4}He + ^{120}Sn) and would be a measurement of the contribution of the direct reaction processes to the total reaction in the case of the exotic ^{6}He projectile.

In table 5, we present the results of the total reaction cross section, and the halo cross section for the four energies. In addition, we compare their difference, identified as fusion cross section with calculations using the Bass potential penetration [101]. We see that the "halo" cross section is quite large, of the order of one-half of the total reaction cross section. This is in contrast with the behaviour of stable systems at low energies, where the direct contribution to the total reaction cross section is usually much smaller.

7.1.3 Total reaction cross sections on targets with mass number $A \approx 60$

The total reaction cross sections of the ^{6}He + ^{58}Ni system obtained from the four-body CDCC calculations have been reduced and are presented in fig. 31, compared with the results for other stable and exotic systems. The first reduction, based on eqs. (8) and (9), was used in this comparison. We see again three bands, the one with lowest reduced reaction cross section corresponds to tightly bound, α-cluster (^{16}O and ^{4}He) projectiles on ^{64}Zn and ^{58}Ni targets, respectively. The one with the highest reduced reaction cross section corresponds to exotic halo nuclei, ^{6}He and ^{8}B, on ^{64}Zn, ^{51}V, and ^{58}Ni targets. The band between both corresponds to reactions of weakly bound, stable (^{6}Li and ^{9}Be) and radioactive (^{8}Li and ^{7}Be) projectiles. A strong enhancement is observed in the total reaction cross section of the exotic ^{6}He projectile compared with tightly bound and weakly bound stable systems. The difference in scale between fig. 30 (logarithmic scale) and fig. 31 (linear scale) could give the wrong impression, that the enhancement is larger for medium targets than for heavy targets, between reaction cross sections of radioactive, halo projectiles, when compared to stable, weakly bound projetiles. If

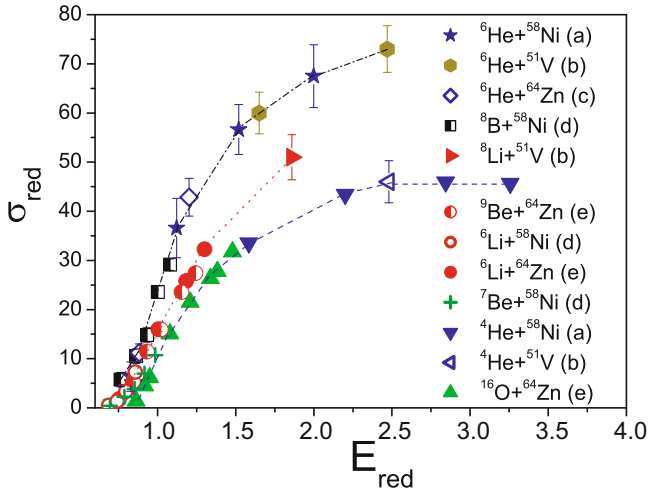

Fig. 31. Reduced reaction cross sections for different projectiles on intermediate mass ($A \approx 60$) targets: (a) from ref. [20, 59, 102], (b) from [55], (c) from [103], (d) from [104] and (e) from [52, 92, 105]. The units of $\sigma_{\rm red}$ and $E_{\rm red}$ are, respectively, mb and MeV. The lines are to guide the eye. Taken from ref. [20].

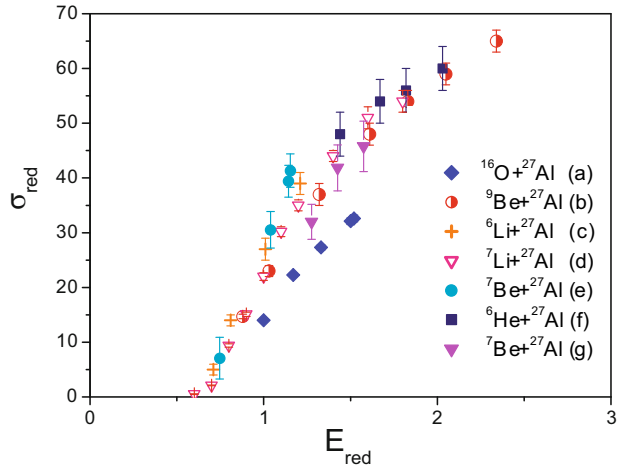

Fig. 32. Reduced reaction cross section for different projectiles on ^{27}Al target [28]: (a) from ref. [106], (b) from [107, 108], (c) from [109], (d) from [110], (e) from [61], (f) from [28] and (g) from [111]. The units of $\sigma_{\rm red}$ and $E_{\rm red}$ are, respectively, mb and MeV. Taken from ref. [32].

one takes the numbers, one sees that the enhancement is about 50% for heavy targets at $E_{\rm red} = 1.2$ MeV, and about 45–50% for the medium mass nuclei at the same reduced energy. Thus the enhancement, mainly due to the coupling to Coulomb break up, is about the same for medium mass and for heavy targets.

7.1.4 Total reaction cross sections with lighter targets: $A = 27$ and $A = 9$

In fig. 32, we present the results of the reduced reaction cross sections obtained from the optical model calculations for ^{6}He and other stable projectiles on an ^{27}Al target. We

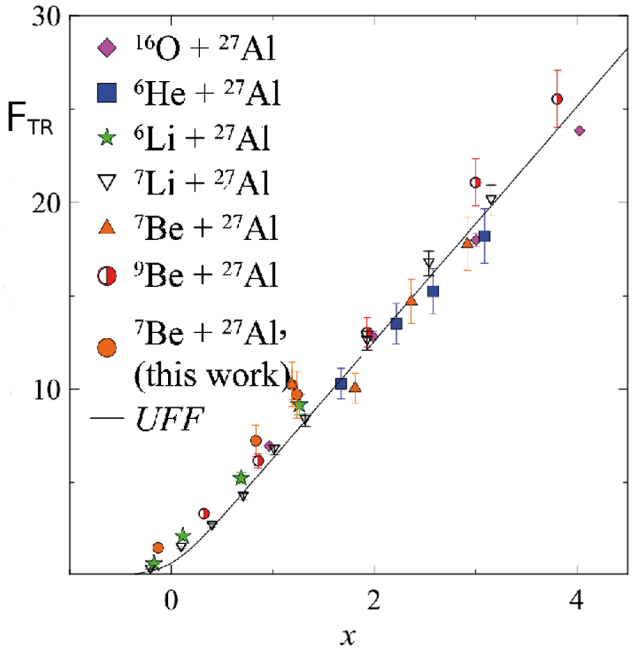

Fig. 33. Total reaction function [28] for different projectiles on ^{27}Al target: (a) from ref. [106], (b) from [107, 108], (c) from [109], (d) from [110], (e) from [61], (f) from [28] and (g) from [111]. Taken from ref. [32].

see that no important enhancement is seen with respect to the weakly bound ^{6,7}Li and ^{9}Be systems; however, all weakly bound (stable or radioactive-halo nuclei) projectiles present a larger reduced reaction cross section than those for the tightly bound ^{16}O projectile. For all systems, the total reaction cross sections have been obtained from optical model calculations using the São Paulo potential. Probably, CDCC calculations should be more adequate for the ^{6}He + ^{27}Al system, since it is known that the coupling to the breakup is very important and should be taken into account. On the other hand, the Coulomb breakup should be less important in the case of the ^{27}Al ($Z = 13$) target than for the systems previously discussed of $A \approx 60$ ($Z \approx 30$) or $A \approx 120$ ($Z \approx 50$), respectively, where the presence of the halo increased considerably the reaction cross section.

In fig. 33, we present the results of the total reaction functions $F_{TR}(\chi)$ (see eq. (13)) derived from a parabolic Coulomb barrier, using the SPP + Coulomb potential for the ^{6}He + ^{27}Al system, compared with other similar stable systems, with weakly bound and tightly bound projectiles. The data are from the same references as in fig. 32. With this reduction, not only the neutron-halo, exotic ^{6}He and the stable, weakly bound projectiles have a very similar reaction function, but even the tightly bound ^{16}O projectile has a similar behaviour. This result is quite surprising and very different from what was observed for the systems with a heavy $A \sim 120$ target.

For the lighter ^{6}He + ^{9}Be system, we are still analyzing the situation but, using the results of the CDCC calculations of sect. 4.4 for the total reaction cross section we observed an enhancement of about 25%, with respect to the

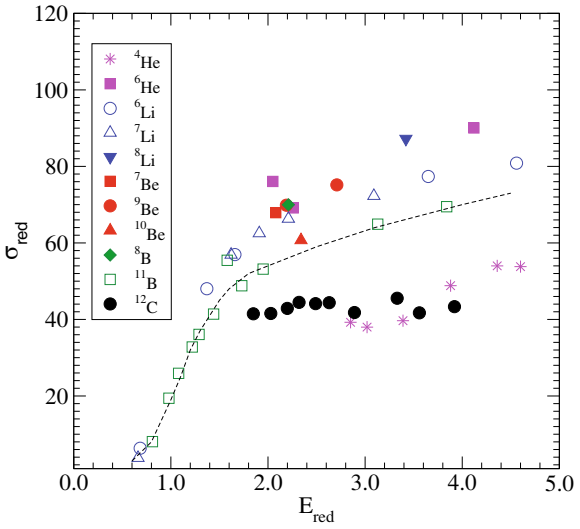

Fig. 34. The reduced reaction cross sections given by eqs. (8) and (9) for the beryllium isotopes and other weakly bound and tightly bound projectiles on ^{12}C. The units of $\sigma_{\rm red}$ and $E_{\rm red}$ are, respectively, mb and MeV. The dashed line is a guide over most of the ^{11}B data points.

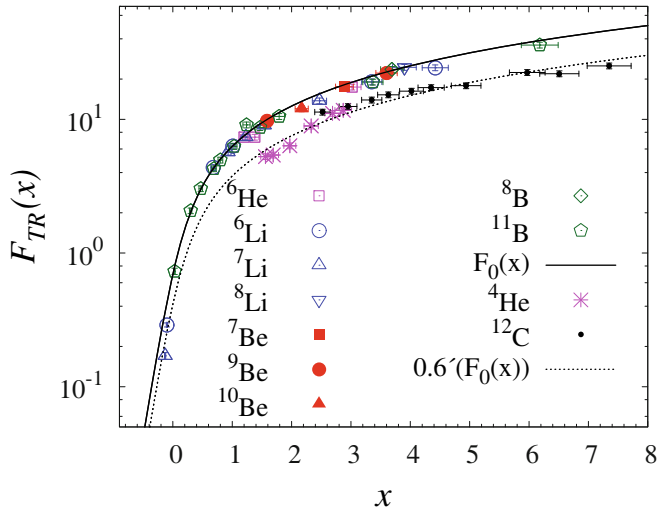

Fig. 35. The total reaction functions considering the universal function $F(\chi)$ for the beryllium isotopes and other weakly bound and tightly bound projectiles on ^{12}C. The solid line is the Universal Fusion Function (UFF) $F_0(\chi) = \ln[1 + e^{2\pi\chi}]$, explained in the text. Taken from ref. [21].

cross section for the weakly bound projectile ^{6}Li. We remark that, in this case, both projectile ^{6}He and target ^{9}Be are weakly bound and that could have an effect, enhancing the total reaction cross section, since the projectile and target can easily break up. Although only the projectile breakup is explicitly taken into account in the CDCC calculations, the empirical optical potentials used to describe the $\alpha + {}^{9}$Be scattering and to build the ^{6}He + ^{9}Be potential used in the CDCC calculations, already contain effects of the target breakup, which could account for a part of the observed enhancement.

For the case of the ^{7}Be projectile on intermediate mass ($A \sim 60$) (see fig. 31) and lighter mass ($A = 27$) (see fig. 32) targets, the total reaction cross sections do not seem to be affected greatly by the lower separation energy of ^{7}Be with respect to other weakly bound nuclei and no significant enhancement has been observed in the reduced reaction cross section with respect to the weakly bound ^{6,7}Li and ^{9}Be.

7.1.5 Total reaction cross sections on carbon targets

For comparison, we have applied both reduction procedures to the total reaction cross sections obtained for several light projectiles, with different binding energies, on a ^{nat}C target.

The reaction cross sections of these many systems come from the following references: for the weakly bound stable projectiles ^{6}Li [112–114], ^{7}Li [112,113], and ^{9}Be [65]; for the no-halo radioactive projectile ^{8}Li [25], for the two-neutron halo ^{6}He [90, 115, 116], and for the proton-halo ^{8}B [63]. The tightly bound, stable projectile ^{11}B + ^{12}C was measured by [117,118]. The reaction cross section for the nuclei with $n\alpha$ structure ^{4}He [119] and ^{12}C [120] on carbon target is also included in fig. 34 and fig. 35.

The results using the first reduction are shown in fig. 34. In fig. 34, a clear separation can be observed between the reduced cross sections of the tightly bound, $n\alpha$ structured projectiles ^{4}He and ^{12}C and the other systems. The tightly bound ^{11}B and ^{10}Be projectiles belong to a different band, with somewhat higher reduced reaction cross section ($\sigma_{\rm red}$) values and the weakly bound, stable, and radioactive, or even, halo projectiles, such as ^{6}He or ^{8}B are situated in still another band of higher reduced reaction cross sections. For $E_{\rm red} \geq 2.0$ even a separation can be observed, between radioactive ^{6}He and ^{8}Li projectiles and the other weakly bound ones. The linear scale of the $\sigma_{\rm red}$ helps to observe these subtle differences, which are not obvious in a logarithmic scale. The trend of tightly bound, non-$n\alpha$ structured projectiles (^{11}B and ^{10}Be) in fig. 34 is guided by the dashed line.

It is interesting to observe that, while for the ^{27}Al target, the neutron halo ^{6}He projectile had similar reduced reaction cross section with the stable or radioactive non-halo projectiles (see figs. 32, 33), for the even lighter ^{12}C and ^{9}Be targets this behaviour is changed and the halo projectile seems to present higher reduced reaction cross sections. We can conjecture about the relative contributions of the Coulomb and nuclear breakup: in the intermediate mass ($A \sim 60$) or heavy ($A \sim 120$) targets, the long range Coulomb interaction is dominant for the breakup process. In the higher-energy region ($E_{\rm red} \geq 2.0$) for the lightest targets ($A = 9$ or 12), the nuclear breakup dominates, and maybe for the $A = 27$ target, there is a destructive interference between both processes, reducing the importance of the breakup process. This hypothesis should be further verified with targets of similar mass.

The parameters V_B, R_B, and ω, necessary for the second reduction procedure, were determined from a parabolic fit of the real optical potentials (see table 2). The values of these parameters are listed in tables II and III

of ref. [21]. Using these parameters, the universal function for the reaction cross section $F_{TR}(\chi)$ was obtained as a function of the reduced energy parameter, χ, for all systems. The results of this reduction for the light projectiles on the ^{12}C target can be seen in fig. 35. This second reduction procedure, by considering the change in the curvature of the barrier, would eliminate the geometric and static effects, with only the dynamic ones remaining, if fusion were the most important contribution to the reaction cross section.

For the second reduction procedure, all systems, with the exception of the tightly bound, $n\alpha$ structured projectiles ^{4}He and ^{12}C, but including projectiles that are weakly bound, stable, or halo nuclei and, even, tightly bound ^{11}B, have similar behaviour and follow the same trend. The evidence that the halo nucleus ^{6}He and the stable and tightly bound ^{10}Be, or ^{11}B present very similar reaction functions on a carbon target is a surprising result. The solid line in fig. 35 corresponds to the so-called universal fusion function (UFF), $F_0(\chi)$. However, the tightly bound, $n\alpha$ structured projectiles ^{4}He and ^{12}C have a different behaviour, with systematically lower reaction cross sections and total reaction function $F_{TR}(\chi)$, being well reproduced by 60% of $F_0(\chi)$.

The difference between the results of both reduction procedures, observed for the light, $n\alpha$ structured carbon target, was not observed for heavy targets ($A \sim 120$) in fig. 30. The decision about which is the best reduction method is still an open debate and we hope that our data and analysis can contribute to elucidate this question.

7.1.6 Comparison of total reaction cross sections of different systems and of different scaling procedures

We have shown experimental evidences that using the first scaling and light mass, low Z (carbon and ^{9}Be), or heavy mass, $A \geq 50$–138, and $Z \geq 30$–50 targets, the reduced reaction cross sections of systems with projectiles of different nature, such as radioactive halo, weakly bound stable or tightly bound stable nuclei, are quite different. If the scaling does not eliminate the differences between the reduced reaction cross sections, this means that there are important reaction mechanisms or processes, which are not described in the scaling. The breakup cross sections of the halo nuclei can be larger than those of the weakly bound stable projectiles, in the long range Coulomb field of the higher Z target nuclei, or in the short range nuclear field of low Z targets at higher energies.

However for targets with $Z = 13$ (^{27}Al) the reduced reaction cross sections of radioactive halo (^{6}He) and weakly bound stable (^{6,7}Li,^{9}Be) projectiles are very similar, but they are larger than those of the tightly bound $n\alpha$ structured ^{16}O projectile. We can imagine a situation where the Coulomb and nuclear break up processes interfere destructively and no enhancement, due to the nuclear halo, is observed.

The results with the second scaling are, surprisingly, not the same. For heavy targets the total reaction functions F_{TR} are quite different for projectiles of different nature (as radioactive halo, weakly bound stable or tightly bound stable nuclei). But for light targets (carbon) the difference between radioactive halo (^{6}He) and weakly bound, stable (^{6,7}Li, ^{9}Be) and tightly bound non-$n\alpha$ structured projectiles (^{11}B, ^{10}Be) disappears with the second scaling. It is hard to understand, how the scaling based on the tunneling concept eliminates the differences between a halo, and a tightly bound projectile. For the ^{27}Al target the second scaling washes out the difference even between the halo (^{6}He), weakly bound, stable (^{6,7}Li, ^{9}Be) and the tightly bound $n\alpha$ structured ^{16}O projectiles. If the main difference between these systems are the facility to break up, or to transfer nucleons, which are both reactions not proceeding by tunneling through the Coulomb barrier, it is hard to understand how the second scaling eliminates the differences between the reaction functions.

All these results indicate the necessity for more measurements but also for more theoretical effort to describe in a consistent way the reaction cross sections between different systems.

7.2 Breakup and alpha-production measurements

7.2.1 Production of α-particles in the ^{6}He + ^{120}Sn collision

In addition to the elastic scattering, a large production of α-particles has been observed in the collision of ^{6}He with several targets in several experiments [22, 121–125]. These α-particles present broad energy distributions, with widths of a few MeV, centered around the velocity of the ^{6}He projectile. In the spectrum of fig. 10, the region where the α-particles appear is indicated (see also ref. [125]). The α-particles can, in principle, be produced in a number of reactions involving the ^{6}He beam. The projectile breakup, one- and two-neutron transfer reactions are possible mechanisms but also complete and incomplete fusion reactions could produce α-particles. For a complete identification of the reaction mechanism, it would be necessary to perform complete coincidence measurements of the neutrons, γ-rays, and α-particles [124]. However, it is still possible to obtain useful information directly from the analysis of the energy and angular distributions of the single α-particles.

In fig. 36, we present the energy distribution (left) and the angular distribution (right) of the α-particles produced in the ^{6}He + ^{120}Sn collision. The cross sections have been calculated in the laboratory system, thus no assumption has been made about any particular reaction mechanism.

In order to improve the statistics, we added the α-yield measured at neighboring angles (55° to 70°). We compare the measured energy distributions with the predictions of the two-neutron transfer to the continuum, breakup, and fusion-evaporation calculations. All calculations have been transformed to the laboratory system, using appropriate Jacobian transformations.

We see that our experimental results agree better with the predictions of two-neutron transfer reactions (solid blue line) rather than the breakup and fusion reactions (dashed and dash-dotted black lines). Transfer reactions

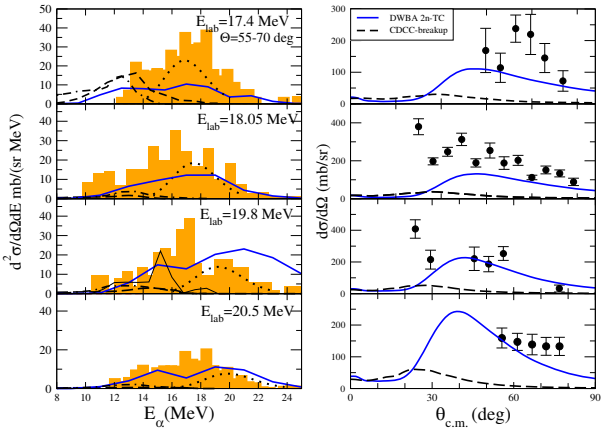

Fig. 36. Energy and angular distributions of α-particles produced in the ^{6}He + ^{120}Sn collision. The dotted black line indicates the position of the optimum Q-window, explained in the text. The solid blue line is the 2 neutron transfer cross section from DWBA calculation, the dashed black line is the breakup cross section from CDCC calculation. Taken from ref. [22].

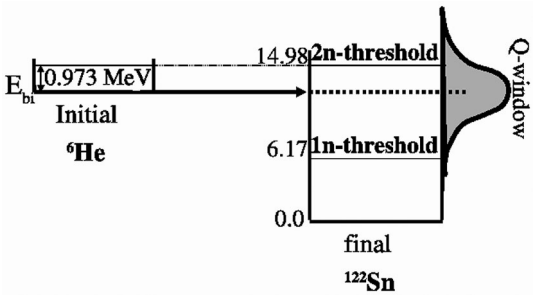

Fig. 37. Scheme of the optimum Q-window for neutron transfer reactions. $E_{\rm bi}$ stands for the binding energy of the ^{6}He nucleus.

are, in general, very selective in terms of the excitation energy of the residual nuclei. The Q-window is determined by the optimum $Q_{\rm opt}$ condition [126] and, for the case of neutron transfers, $Q_{\rm opt} = 0$, which implies that states in the final nucleus around the same binding energy of the projectile will be populated.

In fig. 37, we illustrate the Q-window for the two-neutron transfer reaction ^{120}Sn(^{6}He, α)^{122}Sn. It is centered at an excitation energy of 14.98 MeV in ^{122}Sn, just 0.973 MeV below the two-neutron threshold, but above the one-neutron threshold located at 6.17 MeV excitation energy. This means that the two-neutron transfer reaction will populate mainly states in the continuum of the residual ^{122}Sn nucleus.

The DWBA calculation of the two-neutron transfer to the continuum (TC) is presented in fig. 36 as the solid blue line [22] and it reproduces fairly well the experimental behaviour. In this calculation [127], the continuum of the ^{122}Sn nucleus has been discretized in bins of 1 MeV width up to 9 MeV above the $2n$ threshold. For states below the $2n$ threshold, we used a set of representative states distributed in intervals of 1 MeV following the procedure of Escrig *et al.* [125]. The ^{6}He wave function was calculated in a di-neutron single particle model. The results are compared with the data without any normalization. We see that the agreement is good either from the point of view of the energy distributions or of the shape and magnitude of the angular distributions.

The angle integrated TC cross sections give a value of $\approx$ 650 mb, approximately constant for the four energies analysed. This value is of the order of $\sigma_{\rm halo}$, presented in table 5 and, this is an indication that the α-particles observed around the elastic scattering peak (fig. 10) could account for the enhancement observed in the total reaction cross section for the ^{6}He + ^{120}Sn system, the latter obtained from the elastic scattering angular distribution analysis.

8 Upgrades of the facility

8.1 Large array of neutron detectors

We have available in our laboratory a large-area, position-sensitive neutron detector with neutron/γ-ray discrimination capabilities. This neutron wall was designed to detect intermediate energy neutrons, with kinetic energy of 1 MeV to 100 MeV. It is, then, very useful to perform breakup measurements of neutron-rich nuclei, where the neutrons would be detected in coincidence with the charged particles. This neutron wall is based on the design of the neutron wall of NSCL-Michigan State University [128].

The neutron wall available in the laboratory consists of 25 cylindrical Pyrex cells, filled with an organic-liquid scintillator, NE-213 (Xylene), sealed at both ends, and with a square section of 8 cm^2. The total area is 2×2 m^2, with an inactive area of less than 12%. For a neutron flight distance of 5 m, the wall subtends a solid angle of approximately 20 msr. Detection efficiency of this wall is determined by the areal density of nuclei in the detector and the solid angle coverage, where the thickness of the cell in the beam direction limits the energy resolution. A balance was found between a thick detector, with higher detection efficiency but not so good time resolution, and a distant detector which sacrifices coverage for energy resolution. Photomultipliers (PMTs) are coupled to each end of the cell to detect the scintillated light. The time of an event is determined by the average of the times from the two PMTs, and the position of the neutron incidence is determined by the difference in PMT times. The nominal time resolution is 1 ns, and with a $\sim$ 7.7 cm/ns position to time relation, this leads to a horizontal position resolution similar to the vertical resolution determined by the each cell height (about 7 cm).

To determine the neutron energy, we have to measure the time the neutron takes to travel from the target to the detector. If the length of the flight path is known, we can determine the neutron velocity and energy, regardless of the energy deposited in the detector. However, when

the TOF method is used to determine energy, γ-rays introduce a continuous background in the neutron energy spectrum. To remove the undesired γ-rays, this neutron wall has the capability to perform pulse-shape discrimination (PSD), since the time shape of the pulse for neutrons is different from those for the γ-ray background. This detector will be very useful to use in conjunction with neutron-rich radioactive beams of the RIBRAS system.

8.2 Gamma-ray cave

The detection of gammas in coincidence with particles emitted from reactions is an important step to enhance our capability to separate different reaction channels. However, as the solenoids of RIBRAS have no magnetic shielding, the residual field in the region of the scattering chambers-2 or -3, where the detectors could be mounted, can be as high as tens or even hundreds of Gauss. Magnetic fields of such intensities prevent the use of detectors that depend on electron collection such as ionization chambers, proportional counters, micro-channel plates, and photomultiplier tubes. Only silicon detectors and fast avalanche detectors like parallel plate avalanche counters (PPAC) work in such magnetic fields. Then, in order to operate with the usual gamma detectors, a new scattering chamber will be necessary, distant from the solenoids, in a region where the magnetic field is sufficiently small to not affect photo-multiplier operation. We are planning to make an extension of the RIBRAS beam line to install a gamma cave. In addition, a shield for the neutrons will be necessary since the secondary neutron beam of RIBRAS is intense and could damage the Ge detectors.

9 Conclusions and future perspectives

The research developed in RIBRAS at the present consists mainly of low-energy elastic scattering of light exotic projectiles such as ^{6}He, ^{8}Li, ^{7}Be, ^{8}B, and ^{10}Be on targets of different masses. Elastic scattering at low energies provides information on the interaction potential in these exotic systems, as well as on the total reaction cross section.

For heavy and intermediate mass targets, the Coulomb interaction is very important and long range effects have been observed in the optical potentials derived from the analysis of the elastic scattering of ^{6}He + target. The coupling to the projectile breakup channel was included via continuuum discretized coupled channel calculations (CDCC) and provided a very good description of the experimental data, practically without any parameter adjustment. This indicates that this process is very important and strongly coupled to the elastic channel. The optical potentials derived from the analysis of the ^{6}He scattering and also from CDCC polarization potentials, present a long range tail and the real polarization potential, on the other hand, presents a repulsive component in the region of the surface of the system. These seem to be general characteristics of the optical potentials that describe the scattering data with the ^{6}He projectile and are probably a consequence of the effect of the neutron halo and its low binding energy.

The total reaction cross sections for ^{6}He on heavy and intermediate mass targets, on the other hand, present a clear enhancement compared to the cross section of stable systems (see figs. 30 and 31). The comparison between different systems has to be performed with the reduced reaction cross sections, which take into account the different sizes and different energies with respect to the Coulomb barriers (see eqs. (8) and (9)). When we compare the reduced reaction cross sections from reactions induced by ^{6}He with doubly magic projectiles, such as ^{4}He and ^{16}O, the enhancement is quite large and, even with respect to the weakly bound projectiles ^{6,7}Li and ^{9}Be, enhancements of the order of 50% have been observed. With the reduction based in reaction functions (see eqs. (13) and (11)) the enhancement is still present (see fig. 30), indicating that an important part of the cross section is due to direct, peripheral processes that are not washed out by the reduction based on tunneling through the Coulomb barrier.

For lighter systems, such as ^{6}He + ^{12}C and ^{6}He + ^{9}Be, and at energies well above the Coulomb barrier, the nuclear field dominates and the Coulomb effects may be negligible. The enhancements with respect to the weakly bound systems are reduced but are still of the order of 15–25% of the total reaction cross section, when the first reduction, based on size, charge, and energy differences, is used. Using the second reduction, based on the UFF, the difference between weakly bound and $n\alpha$ structured projectiles can be observed, again indicating the presence of direct processes, contributing to the reaction cross section.

For the ^{27}Al target, the neutron-halo ^{6}He projectile had a reduced reaction cross section similar to the stable, weakly bound or radioactive non-halo projectiles (see figs. 32 and 33), using both reduction methods. Surprisingly, the difference between weakly bound (stable or radioactive, even halo projectiles) and $n\alpha$ structured projectiles (^{16}O) is washed out with this second reduction, based on the UFF concept.

Comparing our results on heavy, intermediate-mass, and light targets, we can conjecture about the relative contributions of the Coulomb and nuclear breakup: in the intermediate mass ($A \sim 60$) or heavy ($A \sim 120$) targets, the long range Coulomb interaction is dominant for the breakup process. In the higher-energy region ($E_{\rm red} \geq 2.0$) for the lightest targets ($A = 9$ or 12), the nuclear breakup dominates and, maybe for the $A = 27$ target, there is a destructive interference between both processes, reducing the importance of the breakup process. This hypothesis should be further verified with targets of similar mass.

These enhancements in the reaction cross section seem to be related to the presence of a high yield of alpha particles produced in the reactions induced by ^{6}He. Such alpha particles have been observed in the ^{6}He + ^{120}Sn scattering, with an energy distribution that indicates that they were

produced in direct processes such as projectile breakup or neutron transfer reactions. The magnitude of the cross sections for the alpha production process seems to account for the observed enhancement in the total reaction cross section of ^{6}He + ^{120}Sn.

The elastic scattering measurements and the deduced total reaction cross sections, obtained with ^{8}Li and ^{7}Be beams, did not present noticeable difference on medium mass target (see ^{8}Li + ^{51}V and ^{7}Be + ^{58}Ni in fig. 31). The difference in their cluster structures did not show up in these systems. However, on lighter target, as ^{12}C, a small enhancement can be observed in the reaction cross section of ^{8}Li and ^{7}Be, when compared to weakly bound, stable projectiles, as ^{6,7}Li (see fig. 34). More data, with better statistics, can shed more light on this problem.

Our most striking results are related to the systematic of the total reaction cross sections on targets of different masses and the good agreement between our elastic scattering data and CDCC calculations. Our recent data on ^{6}He + ^{58}Ni even show a sensitivity to the four-body character of the collision, demanding the exact description of ^{6}He as a core and two correlated neutrons. It is interesting to note that the CDCC calculations, which take only the breakup into account, are able to reproduce the elastic data even in the presence of strong alpha yield, which seems to be more related to transfer reactions than to breakup. These different aspects of the whole complex picture show, that there is still a lot to learn, and the elastic scattering can give many important information.

RIBRAS is now entering in a second phase where we intend to sophisticate our detection system in order to select reaction channels other than elastic scattering. That will require a pulsed primary beam, for time-of-flight measurements, as well as gamma and large area neutron detectors to identify and separate different reaction channels. Recently, we introduced several new improvements in the detection systems of RIBRAS. With the large scattering chamber-3 that entered in operation in 2011, and several new double-sided strip detectors (DSSD), we are able to measure reaction angular distributions with much better angular resolution and higher statistics. The gamma and neutron detectors will become operational in the near future, permitting contributions with new reaction measurements to the field of low-energy, radioactive ion beam science.

The authors thank the participation of their students and postdocs in all stages of the work described in this paper, namely, P.N. de Faria, D.R. Mendes Jr., K.C.C. Pires, A. Barioni, V. Morcelle, J.C. Zamora, M.C. Morais, E. Leistenschneider, R. Pampa Condori, V.B. Scarduelli, E. Benjamin and all of the colleagues who have helped in the measurements or data analysis. Thanks are due to J. Arteche and R. Arteche, who developed the chamber-3. The authors also thank the Fundação de Amparo à Pesquisa do Estado de São Paulo (FAPESP) and the Conselho Nacional de Desenvolvimento Científico e Tecnológico (CNPq) for financial support. The authors thank P. Descouvemont and W.A. Seale for careful reading of the manuscript.

References

1. I. Tanihata, H. Hamagaki, O. Hashimoto, Y. Shida, N. Yoshikawa, K. Sugimoto, O. Yamakawa, T. Kobayashi, N. Takahashi, Phys. Rev. Lett. **55**, 2676 (1985).
2. P.G. Hansen, A.S. Jensen, B. Jonson, Annu. Rev. Nucl. Part. Sci. **45**, 591 (1995).
3. T. Otsuka, R. Fujimoto, Y. Utsuno, B.A. Brown, M. Honma, T. Mizusaki, Phys. Rev. Lett. **87**, 082502 (2001).
4. T. Otsuka, T. Suzuki, R. Fujimoto, H. Grawe, Y. Akaishi, Phys. Rev. Lett. **95**, 232502 (2005).
5. H. Geissel, G. Munzenberg, K. Riisager, Annu. Rev. Nucl. Sci. **45**, 163 (1995).
6. N. Keeley, N. Alamanos, K.W. Kemper, K. Rusek, Progr. Part. Nucl. Phys. **63**, 396 (2009).
7. K. Langanke, M. Wiescher, Rep. Prog. Phys. **64**, 1657 (2001).
8. R. Lichtenthäler, A. Lépine-Szily, V. Guimarães, C. Perego, V. Placco, O. Camargo, R. Denke, P.N. de Faria, E.A. Benjamim, N. Added *et al.*, Eur. Phys. J. A **25**, 733 (2005).
9. M.Y. Lee, F.D. Becchetti, T.W. O'Donnell, D.A. Roberts, J.A. Zimmerman, V. Guimarães, J.J. Kolata, D. Peterson, P. Santi, P.A. DeYoung *et al.*, Nucl. Instrum. Methods A **422**, 536 (1999).
10. O. Sala, G. Spalek, Nucl. Instrum. Methods **112**, 213 (1974).
11. A. Lépine-Szily, R. Lichtenthäler, V. Guimarães, Nucl. Phys. News **23**, 5 (2013).
12. K.C.C. Pires, R. Lichtenthäler, A. Lépine-Szily, V. Guimarães, P.N. de Faria, A. Barioni, D.R. Mendes Junior, V. Morcelle, R. Pampa Condori, M.C. Morais *et al.*, Phys. Rev. C **83**, 064603 (2011).
13. D.R. Mendes, A. Lépine-Szily, P. Descouvemont, R. Lichtenthäler, V. Guimarães, P.N. de Faria, A. Barioni, K.C.C. Pires, V. Morcelle, R. Pampa Condori *et al.*, Phys. Rev. C **86**, 064321 (2012).
14. C. Granja, J. Jakubek, P.N. de Faria, R. Lichtenthäler, A. Lépine-Szily, S. Pospíšil, IEEE NSS/MIC Proc. Conf. Record **2011**, 1918 (2011).
15. M.Y. Lee, PhD thesis, University of Michigan (2002).
16. R. Lichtenthaler, private communication.
17. E. Leistenschneider, A. Lepine-Szily, R. Lichtenthaeler, AIP Conf. Proc. **1529**, 206 (2013).
18. I. Antcheva, M. Ballintijn, B. Bellenot, M. Biskup, R. Brun, N. Buncic, P. Canal, D. Casadei, O. Couet, V. Fine *et al.*, Comput. Phys. Commun. **180**, 2499 (2009).
19. R. Lichtenthäler, R.P. Condori, P.N. de Faria, A. Lépine-Szily, D.R. Mendes, Jr., K.C.C. Pires, M.C. Morais, E. Leistenschneider, V.B. Scarduelli, J.M.B. Shorto *et al.*, AIP Conf. Proc. **1529**, 197 (2013).
20. V. Morcelle, K.C.C. Pires, M. Rodríguez-Gallardo, R. Lichtenthäler, A. Lépine-Szily, V. Guimarães, P.N. de Faria, D.R. Mendes, Jr., A.M. Moro, L.R. Gasques *et al.*, Phys. Lett. B **732**, 228 (2014).
21. J.C. Zamora, V. Guimarães, A. Barioni, A. Lépine-Szily, R. Lichtenthäler, P.N. de Faria, D.R. Mendes, L.R. Gasques, J.M.B. Shorto, V. Scarduelli *et al.*, Phys. Rev. C **84**, 034611 (2011).
22. P.N. de Faria, R. Lichtenthäler, K.C.C. Pires, A.M. Moro, A. Lépine-Szily, V. Guimarães, D.R. Mendes, A. Arazi, A. Barioni, V. Morcelle *et al.*, Phys. Rev. C **82**, 034602 (2010).

23. P.N. de Faria, R. Lichtenthäler, K.C.C. Pires, A.M. Moro, A. Lépine-Szily, V. Guimarães, D.R. Mendes, A. Arazi, M. Rodríguez-Gallardo, A. Barioni *et al.*, Phys. Rev. C **81**, 044605 (2010).
24. S. Mukherjee, N.N. Deshmukh, V. Guimarães, J. Lubian, P.R.S. Gomes, A. Barioni, S. Appannababu, C.C. Lopes, E.N. Cardozo, K.C.C. Pires *et al.*, Eur. Phys. J. A **45**, 23 (2010).
25. A. Barioni, V. Guimarães, A. Lépine-Szily, R. Lichtenthäler, D.R. Mendes, Jr., E. Crema, K.C.C. Pires, M.C. Morais, V. Morcelle, P.N. de Faria *et al.*, Phys. Rev. C **80**, 034617 (2009).
26. R. Lichtenthäler, P.N. de Faria, A. Lépine-Szily, V. Guimarães, O. Camargo, Jr., R. Denke, E.A. Benjamim, A. Barioni, K.C.C. Pires, D.J. Mendes *et al.*, Eur. Phys. J.-S-T **150**, 27 (2007).
27. RIBRAS Collaboration (A. Lépine-Szily, R. Lichtenthäler), Nucl. Phys. A **787**, 94C (2007).
28. E.A. Benjamim, A. Lépine-Szily, D.R. Mendes, Jr., R. Lichtenthäler, V. Guimarães, P.R.S. Gomes, L.C. Chamon, M.S. Hussein, A.M. Moro, A. Arazi *et al.*, Phys. Lett. B **647**, 30 (2007).
29. L.F. Canto, M.S. Hussein, *Scattering Theory of Molecules, Atoms and Nuclei* (World Scientific Publishing, 2013).
30. W.E. Frahn, Phys. Rev. Lett. **26**, 568 (1970).
31. R. Lichtenthaler, private communication.
32. V. Morcelle, R. Lichtenthäler, R. Linares, M.C. Morais, V. Guimarães, A. Lépine-Szily, P.R.S. Gomes, J. Lubian, D.R. Mendes, Jr., P.N. de Faria *et al.*, Phys. Rev. C **89**, 044611 (2014).
33. W.T. Milner, ORNL Report, **100** (1987).
34. H. Feshbach, *Theoretical Nuclear Physics* (Wiley & Sons Publishing, 1992).
35. G.R. Satchler, W.G. Love, Phys. Rep. **55**, 183 (1979).
36. L.C. Chamon, B.V. Carlson, L.R. Gasques, D. Pereira, C. De Conti, M.A.G. Alvarez, M.S. Hussein, M.A. Cândido Ribeiro, E.S. Rossi, C.P. Silva, Phys. Rev. C **66**, 014610 (2002).
37. M.A.G. Alvarez, L.C. Chamon, M.S. Hussein, D. Pereira, L.R. Gasques, E.S. Rossi, C.P. Silva, Nucl. Phys. A **723**, 93 (2003).
38. B.V. Carlson, D. Hirata, Phys. Rev. C **62**, 054310 (2000).
39. N. Austern, Y. Iseri, M. Kamimura, M. Kawai, G. Rawitscher, M. Yahiro, Phys. Rep. **154**, 125 (1987).
40. E.F. Aguilera, J.J. Kolata, F.M. Nunes, F.D. Becchetti, P.A. DeYoung, M. Goupell, V. Guimarães, B. Hughey, M.Y. Lee, D. Lizcano *et al.*, Phys. Rev. Lett. **84**, 5058 (2000).
41. E.F. Aguilera, J.J. Kolata, F.D. Becchetti, P.A. DeYoung, J.D. Hinnefeld, A. Horváth, L.O. Lamm, H.Y. Lee, D. Lizcano, E. Martinez-Quiroz *et al.*, Phys. Rev. C **63**, 061603 (2001).
42. N. Keeley, J.M. Cook, K.W. Kemper, B.T. Roeder, W.D. Weintraub, F. Maréchal, K. Rusek, Phys. Rev. C **68**, 054601 (2003).
43. O.R. Kakuee, J. Rahighi, A.M. Sánchez-Benitez, M.V. Andrés, S. Cherubini, T. Davinson, W. Galster, J. Gómez-Camacho, A.M. Laird, M. Lamehi-Rachti *et al.*, Nucl. Phys. A **728**, 339 (2003).
44. M.S. Hussein, R. Lichtenthäler, F.M. Nunes, I.J. Thompson, Phys. Lett. B **640**, 91 (2006).
45. T. Matsumoto, T. Egami, K. Ogata, Y. Iseri, M. Kamimura, M. Yahiro, Phys. Rev. C **73**, 051602 (2006).
46. M. Rodríguez-Gallardo, J.M. Arias, J. Gómez-Camacho, R.C. Johnson, A.M. Moro, I.J. Thompson, J.A. Tostevin, Phys. Rev. C **77**, 064609 (2008).
47. M. Rodríguez-Gallardo, J.M. Arias, J. Gómez-Camacho, A.M. Moro, I.J. Thompson, J.A. Tostevin, Phys. Rev. C **80**, 051601 (2009).
48. A.M. Moro, K. Rusek, J.M. Arias, J. Gómez-Camacho, M. Rodríguez-Gallardo, Phys. Rev. C **75**, 064607 (2007).
49. I.J. Thompson, Comp. Phys. Rep. **17**, 167 (1998).
50. M.A. Nagarajan, C. Mahaux, G.R. Satchler, Phys. Rev. Lett. **54**, 1136 (1985).
51. C. Mahaux, H. Ng, G.R. Satchler, Nucl. Phys. A **449**, 354 (1986).
52. P.R.S. Gomes, M.D. Rodríguez, G.V. Martí, I. Padron, L.C. Chamon, J.O. Fernández Niello, O.A. Capurro, A.J. Pacheco, J.E. Testoni, A. Arazi *et al.*, Phys. Rev. C **71**, 034608 (2005).
53. M.S. Hussein, P.R.S. Gomes, J. Lubian, L.C. Chamon, Phys. Rev. C **73**, 044610 (2006).
54. U. Arlt, R. Bass, V. Hartmann, R. Renfordt, K. Sapotta, P. Fröbrich, W. Schäfer, Phys. Rev. C **22**, 1790 (1980).
55. V. Morcelle, Master's thesis, IFUSP (2007).
56. H. de Vries, C.W. de Jager, C. de Vries, At. Data Nucl. Data Tables **36**, 495 (1987).
57. M. Majer, R. Raabe, M. Milin, C. Angulo, J. Cabrera, E. Casarejos, J.L. Charvet, D. Escrig, A. Gillibert, T. Keutgen *et al.*, Eur. Phys. J. A **43**, 153 (2010).
58. L.R. Gasques, L.C. Chamon, D. Pereira, V. Guimarães, A. Lépine-Szily, M.A.G. Alvarez, E.S. Rossi, C.P. Silva, B.V. Carlson, J.J. Kolata *et al.*, Phys. Rev. C **67**, 024602 (2003).
59. L.R. Gasques, L.C. Chamon, D. Pereira, M.A.G. Alvarez, E.S. Rossi, C.P. Silva, G.P.A. Nobre, B.V. Carlson, Phys. Rev. C **67**, 067603 (2003).
60. G.D. Alkhazov, M.N. Andronenko, A.V. Dobrovolsky, P. Egelhof, G.E. Gavrilov, H. Geissel, H. Irnich, A.V. Khanzadeev, G.A. Korolev, A.A. Lobodenko *et al.*, Phys. Rev. Lett. **78**, 2313 (1997).
61. V. Morcelle, PhD thesis, IFUSP (2012).
62. R. Lichtenthäler, Rev. Mex. Fis. **53**, 59 (2007).
63. A. Barioni, J.C. Zamora, V. Guimarães, B. Paes, J. Lubian, E.F. Aguilera, J.J. Kolata, A.L. Roberts, F.D. Becchetti, A. Villano *et al.*, Phys. Rev. C **84**, 014603 (2011).
64. B. Kamys, L. Jarczyk, Z. Rudy, A. Strzalkowski, H.H. Wolter, J. Lang, R. Müller, J. Sromicki, Nucl. Phys. A **406**, 193 (1983).
65. L. Jarczyk, J. Okolowicz, A. Strzalkowski, K. Bodek, M. Hugi, L. Lang, R. Müller, E. Ungricht, Nucl. Phys. A **316**, 139 (1979).
66. C.M. Perey, F.G. Perey, At. Data Nucl. Data Tables **17**, 1 (1976).
67. U. Schwinn, G. Mairle, G. Wagner, C. Rämer, Z. Physik, A **275**, 241 (1975).
68. G.B. Liu, H.T. Fortune, Phys. Rev. C **38**, 1985 (1988).

69. O. Camargo, V. Guimarães, R. Lichtenthäler, V. Scarduelli, J.J. Kolata, C.A. Bertulani, H. Amro, F.D. Becchetti, H. Jiang, E.F. Aguilera *et al.*, Phys. Rev. C **78**, 034605 (2008).
70. S. Jun, L. Zhi-Hong, G. Bing, L. Wei-Ping, B. Xi-Xiang, Z. Sheng, L. Gang, Y. Sheng-Quan, W. Bao-Xiang, W. You-Bao, Chin. Phys. Lett. **23**, 55 (2006).
71. M.B. Tsang, J. Lee, W.G. Lynch, Phys. Rev. Lett. **95**, 222501 (2005).
72. S. Cohen, D. Kurath, Nucl. Phys. A **101**, 1 (1967).
73. B. Brown, A. Etchegoyen, W. Rae, Report **524** (1998).
74. P. Mohr, P.N. de Faria, R. Lichtenthäler, K.C.C. Pires, V. Guimarães, A. Lépine-Szily, D.R. Mendes, A. Arazi, A. Barioni, V. Morcelle *et al.*, Phys. Rev. C **82**, 044606 (2010).
75. U. Atzrott, P. Mohr, H. Abele, C. Hillenmayer, G. Staudt, Phys. Rev. C **53**, 1336 (1996).
76. P. Mohr, Phys. Rev. C **62**, 061601 (2000).
77. D.R. Tilley, J.H. Kelley, J.L. Godwin, D.J. Millener, J.E. Purcell, C.G. Sheu, H.R. Weller, Nucl. Phys. A **745**, 155 (2004).
78. G.V. Rogachev, P. Boutachkov, A. Aprahamian, F.D. Becchetti, J.P. Bychowski, Y. Chen, G. Chubarian, P.A. DeYoung, V.Z. Goldberg, J.J. Kolata *et al.*, Phys. Rev. Lett. **92**, 232502 (2004).
79. R.P. Condori, R. Lichtenthäler, P.N. de Faria, A. Lépine-Szily, D.R. Mendes, Jr., K.C.C. Pires, M.C. Morais, E. Leistenschneider, V.B. Scarduelli, J.M.B. Shorto *et al.*, EPJ Web of Conferences **66**, 03054 (2014).
80. J.P. Glickman, W. Bertozzi, T.N. Buti, S. Dixit, F.W. Hersman, C.E. Hyde-Wright, M.V. Hynes, R.W. Lourie, B.E. Norum, J.J. Kelly *et al.*, Phys. Rev. C **43**, 1740 (1991).
81. S. Dixit, W. Bertozzi, T.N. Buti, J.M. Finn, F.W. Hersman, C.E. Hyde-Wright, M.V. Hynes, M.A. Kovash, B.E. Norum, J.J. Kelly *et al.*, Phys. Rev. C **43**, 1758 (1991).
82. A.M. Lane, R.G. Thomas, Rev. Mod. Phys. **30**, 257 (1958).
83. P. Descouvemont, D. Baye, Rep. Prog. Phys. **73**, 036301 (2010).
84. H. Ishiyama, T. Hashimoto, K. Yamaguchi, Y. Watanabe, N. Imai, Y. Hirayama, H. Miyatake, M.H. Tanaka, N. Yoshikawa, S. Jeong *et al.*, AIP Conf. Proc. **1120**, 177 (2009).
85. J.F. Lara, T. Kajino, G.J. Mathews, Phys. Rev. D **73**, 083501 (2006).
86. M. La Cognata, A. Del Zoppo, Astrophys. J. **736**, 148 (2011).
87. T. Sasaqui, K. Otsuki, T. Kajino, G.J. Mathews, Astrophys. J. **645**, 1345 (2006).
88. F.D. Becchetti, J.A. Brown, W.Z. Liu, J.W. Jänecke, D.A. Roberts, J.J. Kolata, R.J. Smith, K. Lamkin, A. Morsad, R.E. Warner *et al.*, Nucl. Phys. A **550**, 507 (1992).
89. P. Paul, D. Kohler, Phys. Rev. **129**, 2698 (1963).
90. E.F. Aguilera, I. Martel, A.M. Sánchez-Benítez, L. Acosta, Phys. Rev. C **83**, 021601 (2011).
91. P.R.S. Gomes, L.F. Canto, J. Lubian, M.S. Hussein, Phys. Lett. B **695**, 320 (2011).
92. P.R.S. Gomes, I. Padron, M.D. Rodriguez, G.V. Marti, R.M. Anjos, J. Lubian, R. Veiga, R. Liguori Neto, E. Crema, N. Added *et al.*, Phys. Lett. B **601**, 20 (2004).
93. P.R.S. Gomes, J. Lubian, I. Padron, R.M. Anjos, Phys. Rev. C **71**, 017601 (2005).
94. L.F. Canto, P.R.S. Gomes, J. Lubian, L.C. Chamon, E. Crema, Nucl. Phys. A **821**, 51 (2009).
95. J.M.B. Shorto, P.R.S. Gomes, J. Lubian, L.F. Canto, S. Mukherjee, L.C. Chamon, Phys. Lett. B **678**, 77 (2009).
96. L.F. Canto, P.R.S. Gomes, J. Lubian, L.C. Chamon, E. Crema, J. Phys. G **36**, 015109 (2009).
97. C.Y. Wong, Phys. Rev. Lett. **31**, 766 (1973).
98. P.N. de Faria, PhD thesis, IFUSP (2009).
99. A.M.M. Maciel, P.R.S. Gomes, J. Lubian, R.M. Anjos, R. Cabezas, G.M. Santos, C. Muri, S.B. Moraes, R. Liguori Neto, N. Added *et al.*, Phys. Rev. C **59**, 2103 (1999).
100. C.P. Silva, M.A.G. Alvarez, L.C. Chamon, D. Pereira, M.N. Rao, E.S. Rossi Jr., L.R. Gasques, M.A.E. Santo, R.M. Anjos, J. Lubian *et al.*, Nucl. Phys. A **679**, 287 (2001).
101. R. Bass, Phys. Rev. Lett. **39**, 265 (1977).
102. L.R. Gasques, L.C. Chamon, P.R.S. Gomes, J. Lubian, Nucl. Phys. A **764**, 135 (2006).
103. A. Di Pietro, P. Figuera, F. Amorini, C. Angulo, G. Cardella, S. Cherubini, T. Davinson, D. Leanza, J. Lu, H. Mahmud *et al.*, Europhys. Lett. **64**, 309 (2003).
104. E.F. Aguilera, E. Martinez-Quiroz, D. Lizcano, A. Gomez-Camacho, J.J. Kolata, L.O. Lamm, V. Guimaraes, R. Lichtenthaler, O. Camargo, F.D. Becchetti *et al.*, Phys. Rev. C **79**, 021601 (2009).
105. S.B. Moraes, P.R.S. Gomes, J. Lubian, J.J.S. Alves, R.M. Anjos, M.M. Sant'Anna, I. Padrón, C. Muri, R. Liguori Neto, N. Added, Phys. Rev. C **61**, 064608 (2000).
106. E. Crema, Master's thesis, IFUSP (1979).
107. P.R.S. Gomes, R.M. Anjos, C. Muri, J. Lubian, I. Padron, L.C. Chamon, R.L. Neto, N. Added, J.O. Fernández Niello, G.V. Martí *et al.*, Phys. Rev. C **70**, 054605 (2004).
108. G.V. Marti, P.R.S. Gomes, M.D. Rodriguez, J.O.F. Niello, O.A. Capurro, A.J. Pacheco, J.E. Testoni, M. Ramirez, A. Arazi, I. Padron *et al.*, Phys. Rev. C **71**, 027602 (2005).
109. J.M. Figueira, J.O.F. Niello, D. Abriola, A. Arazi, O.A. Capurro, E. de Barbara, G.V. Marti, D.M. Heimann, A.E. Negri, A.J. Pacheco *et al.*, Phys. Rev. C **75**, 017602 (2007).
110. J.M. Figueira, D. Abriola, J.O.F. Niello, A. Arazi, O.A. Capurro, E.d. Barbará, G.V. Martí, D. Martínez Heimann, A.J. Pacheco, J.E. Testoni *et al.*, Phys. Rev. C **73**, 054603 (2006).
111. K. Kalita, S. Verma, R. Singh, J.J. Das, A. Jhingan, N. Madhavan, S. Nath, T. Varughese, P. Sugathan, V.V. Parkar *et al.*, Phys. Rev. C **73**, 024609 (2006).
112. J.E. Poling, E. Norbeck, R.R. Carlson, Phys. Rev. C **5**, 1819 (1972).
113. J.E. Poling, E. Norbeck, R.R. Carlson, Phys. Rev. C **13**, 648 (1976).
114. D.E. Trcka, A.D. Frawley, K.W. Kemper, D. Robson, J.D. Fox, E.G. Myers, Phys. Rev. C **41**, 2134 (1990).

115. R.E. Warner, F.D. Becchetti, J.W. Jänecke, D.A. Roberts, D. Butts, C.L. Carpenter, J.M. Fetter, A. Muthukrishnan, J.J. Kolata, K. Lamkin *et al.*, Phys. Rev. C **51**, 178 (1995).
116. R.J. Smith, J.J. Kolata, K. Lamkin, A. Morsad, K. Ashktorab, F.D. Becchetti, J.A. Brown, J.W. Janecke, W.Z. Liu, D.A. Roberts, Phys. Rev. C **43**, 761 (1991).
117. L. Jarczyk, B. Kamys, A. Strzalkowski, A. Szczurek, M. Godlewski, J. Lang, R. Müller, J. Sromicki, Phys. Rev. C **31**, 12 (1985).
118. A.T. Rudchik, A. Budzanowski, V.K. Chernievsky, B. Czech, L. Glowacka, S. Kliczewski, A.V. Mokhnach, O.A. Momotyuk, S.E. Omelchuk, V.M. Pirnak *et al.*, Nucl. Phys. A **695**, 51 (2001).
119. E.B. Carter, G.E. Mitchell, R.H. Davis, Phys. Rev. B **133**, 1421 (1964).
120. R.J. Ledoux, M.J. Bechara, C.E. Ordonez, H.A. Al-Juwair, E.R. Cosman, Phys. Rev. C **27**, 1103 (1983).
121. J.P. Bychowski, P.A. DeYoung, B.B. Hilldore, J.D. Hinnefeld, A. Vida, F.D. Becchetti, J. Lupton, T.W. O'Donnell, J.J. Kolata, G. Rogachev *et al.*, Phys. Lett. B **596**, 26 (2004).
122. J.J. Kolata, H. Amro, F.D. Becchetti, J.A. Brown, P.A. DeYoung, M. Hencheck, J.D. Hinnefeld, G.F. Peaslee, A.L. Fritsch, C. Hall *et al.*, Phys. Rev. C **75**, 031302 (2007).
123. P.A. DeYoung, P.J. Mears, J.J. Kolata, E.F. Aguilera, F.D. Becchetti, Y. Chen, M. Cloughesy, H. Griffin, C. Guess, J.D. Hinnefeld *et al.*, Phys. Rev. C **71**, 051601 (2005).
124. A. Chatterjee, A. Navin, A. Shrivastava, S. Bhattacharyya, M. Rejmund, N. Keeley, V. Nanal, J. Nyberg, R.G. Pillay, K. Ramachandran *et al.*, Phys. Rev. Lett. **101**, 032701 (2008).
125. D. Escrig, A.M. Sanchez-Benitez, A.M. Moro, M.A.G. Alvarez, M.V. Andres, C.C. Angulo, M.J.G. Borge, J. Cabrera, S. Cherubini, P. Demaret *et al.*, Nucl. Phys. A **792**, 2 (2007).
126. D.M. Brink, Phys. Lett. B **40**, 37 (1972).
127. A.M. Moro, F.M. Nunes, D. Escrig, J. Gómez-Camacho, Nucl. Phys. A **787**, 463 (2007).
128. P.D. Zecher, A. Galonsky, J.J. Kruse, S.J. Gaff, J. Ottarsona, J. Wang, F. Deikb, A. Horvath, A. Kiss, Z. Seres *et al.*, Nucl. Instrum. Methods A **401**, 329 (1997).

Alinka Lépine-Szily is an experimental nuclear physicist working in the field of reactions and structure of radioactive nuclei, currently a senior professor at University of São Paulo (USP). She was director of Open Laboratory of Nuclear Physics (LAFN) of USP from 2007 to 2011. She participated actively in the acquisition and installation of the RIBRAS facility. She is chair of the Nuclear Physics Commission (C12) of IUPAP, co-chair of Latin American Association of Nuclear Physics and Applications (ALAFNA) and member of the Hungarian Academy of Sciences.

Rubens Lichtenthäler Filho, is a nuclear physicist working in the field of nuclear reactions with secondary beams of exotic nuclei. Made his graduation, MSc and PhD at the University of São Paulo and post doctoral research at Laboratory GANIL, France. He is one of the physicists responsible for the installation of the Radioactive Ion Beams in Brasil (RIBRAS) facility and is, presently, the coordinator of the RIBRAS system.

Valdir Guimarães is an experimental nuclear physicist working in radioactive ion beam production, elastic scattering, transfer, breakup, fusion and fission reactions measurements, spectroscopic investigation of light unstable nuclei and on the study of nuclear reactions with interest to nuclear astrophysics. He got his PhD at University of Sao Paulo and he was post-doctoral research fellow at University of Tokyo (1994–1995) in Japan and at University of Notre Dame in USA (1997–2000). He is now working at the Instituto de Física da Universidade de São Paulo.